Magnetic Resonance Spectroscopy Quality Assessment at CUBIC and Application to the Study of the Cerebellar Deep Nuclei in children with Fetal Alcohol Spectrum Disorder

Lindie du Plessis

Supervisor: Associate Professor EM Meintjes

Thesis submitted to the Faculty of Health Sciences at the University of Cape Town in partial fulfilment of the requirements for the degree of Master of Science in Biomedical Engineering.

Cape Town, February 2010

Declaration

I, LINDIE DU PLESSIS, hereby declare that the work on which this thesis is based is my own original work (except where acknowledgements indicate otherwise) and that neither the whole, nor any part of it, has been, or is to be submitted for any other degree in this or any other University.

I empower the University to reproduce for the purpose of research either the whole or part of the contents of this thesis in any manner.

_____

Signature

_____

Date

Abstract

In vivo magnetic resonance spectroscopy (MRS) is an imaging technique that allows the chemical study of human tissue non-invasively. The method holds great promise as a diagnostic tool once its reliability has been established. Inter-scanner variability has, however, hampered this from happening as results cannot easily be compared if acquired on different scanners.

In this study a phantom was constructed to determine the localisation efficiency of the 3 T Siemens Allegra MRI scanner located at the Cape Universities Brain Imaging Centre (CUBIC). Sufficient localisation is the key to acquiring useful spectroscopic data as only the signal from a small volume of interest (VOI) is typically acquired. The phantom consisted of a Perspex cube located inside a larger Perspex sphere. Solutions of the cerebral metabolites N-acetyl aspartate (NAA) and choline (Cho) were placed in the inner cube and outer sphere respectively. The phantom was scanned at a range of voxel sizes and echo times in order to determine parameters that typically indicate the performance of the scanner in question.

The resultant full width at half maximum (FWHM) and signal to noise ratio (SNR) values indicated that optimal results were obtained for a voxel with dimensions 20 x 20 x 20 mm^3. The selection efficiency could not be measured due to limitations in the scanner, but two other performance parameters – extra volume suppression (EVS) and contamination – could be determined. The EVS showed that the scanner was able to eliminate the entire background signal from the out-of-voxel region when voxel sizes with dimensions $(20\ mm)^3$ and $(30\ mm)^3$ were used. This performance decreased to 96.2% for a voxel size of $(50\ mm)^3$. The contamination indicated that the unwanted signal, weighted by the respective proton densities of the chemicals, ranged from 12% in the $(20\ mm)^3$ voxel to 24% in the $(50\ mm)^3$ voxel. These ranges are well within acceptable limits for proton MRS.

Analysis of the water suppression achieved in the scanner showed an efficiency of 98.84%, which is acceptable for proton spectroscopy. It was also found that manual

shimming of the scanner improved the spectra obtained, as compared to the automated shimming performed by the scanner.

The second objective of the study was to quantify absolute metabolite concentrations in the familiar SI units of mM as results were previously mostly expressed as metabolite ratios. The LCModel software was used to assess two methods of determining absolute metabolite concentrations and the procedure using water scaling consistently showed superior performance to a method using a calibration factor.

The method employing water scaling was then applied to a study of fetal alcohol spectrum disorder (FASD) where the deep cerebellar nuclei of children with FASD and a control group were scanned. The cerebellar nuclei were of interest as children with FASD show a remarkably consistent deficit in eye blink conditioning (EBC). The cerebellar deep nuclei is known to play a critical role in the EBC response.

The results show significant decreases in the myo-inositol (mI) and total choline (tCho) concentrations of children with FASD in the deep cerebellar nuclei compared to control children. The FAS/PFAS subjects have a mean mI concentration of 4.6 mM as compared to a mean of 5.3 mM in the controls. A Pearson correlation showed that there was a significant relationship between decreasing mI concentrations with increasing prenatal alcohol exposure. The mean tCho concentrations are 1.3 mM for FAS/PFAS and 1.5 mM for the controls. There was no significant differences between the heavily exposed group and either the FAS/PFAS or the control subjects for either metabolite.

The decreased mI and tCho concentrations may indicate deficient calcium signalling or decreased cell membrane integrity – both of which can explain the compromised cerebellar learning in FASD subjects.

Keywords: magnetic resonance spectroscopy; magnetic resonance imaging; metabolites; phantom; myo-inositol; fetal alcohol spectrum disorder (FASD)

Acknowledgements

I hereby wish to express my gratitude to the following individuals who enabled this document to be successfully and timeously completed:

- Associate Professor Ernesta Meintjes for guidance and input with the project
- The NRF for funding the project
- Bruce Spottiswoode and the CUBIC staff for assistance with the phantom experiments
- Aaron Hess for pulse sequence support
- Professors Sue Kidson and Laurie Kellaway for the use of the chemistry laboratories
- Steven Provencher for assistance with the LCModel software

Table of Contents

Declaration ii
Abstract iii
Acknowledgements v
Table of Contents vi
I. List of Abbreviations ix
II. List of Symbols xii
III. List of Figures xiv
IV. List of Tables xvi

1. Introduction 1
2. MRS Principles 2
2.1 General 2
2.2 Precession of Spins 3
2.3 Chemical Shielding and Chemical Shift 4
2.4 Spin Configurations and Spin-Spin Splitting 5
2.5 Cerebral Metabolites of Interest in MRS 8
3. MRS Pulse Sequences 11
3.1 Point Resolved Spectroscopy (PRESS) 12
3.2 Stimulated Echo Acquisition Mode (STEAM) 13
3.3 Water Suppression 14
3.4 Signal Losses and Contamination 16
4. Linear Combination Modeling and LCModel 17
5. Methods 19
5.1 Localisation Phantom 19
5.2 Assessing Accuracy and Localisation 21
5.3 Other Performance Parameters 24
5.4 Determination of Absolute Metabolite Concentrations 24
5.4.1 Calibration Factor 24
5.4.2 Water Scaling 25

5.4.3 Partial Volume Correction 26
5.5 Data Acquisition and Processing 27
5.5.1 Scanner Performance 27
5.5.2 Absolute Metabolite Concentrations 30
6. Phantom Results 31
6.1 Localisation Phantom 31
6.1.1 General 31
6.1.2 Resolution and Signal-to-Noise Ratio 31
6.1.3 Selection Efficiency 33
6.1.4 Extra Volume Suppression 35
6.1.5 Contamination 37
6.1.6 Water Suppression 39
6.1.7 Manual vs. Auto-Shimming 40
6.2 Absolute Metabolite Concentration Phantom 43
6.2.1 Calibration Factor 43
6.2.2 Water Scaling 44
7. Discussion of Phantom Results 45
7.1 Localisation Phantom 45
7.1.1 Resolution and Signal-to-Noise Ratio 45
7.1.2 Selection Efficiency 46
7.1.3 Extra Volume Suppression 48
7.1.4 Contamination 48
7.1.5 Water Suppression 49
7.1.6 Manual vs. Auto-Shimming 49
7.2 Absolute Metabolite Concentration Phantom 50
7.2.1 Calibration Factor 50
7.2.2 Water Scaling 50
8. MRS study of the cerebellar deep nuclei in children with Fetal Alcohol Spectrum Disorder. 52
8.1 Introduction 52
8.2 Background 52

8.2.1 Fetal Alcohol Spectrum Disorder 52
8.2.2 Neuroimaging of FASD 54
8.3 Methods 62
8.4 Results 67
8.4.1 Partial Volume Correction 67
8.4.2 Absolute Metabolite Concentrations in the Cerebellar Nuclei 68
8.5 Discussion 70
8.5.1 Partial Volume Correction 70
8.5.2 Absolute Metabolite Concentrations in the Cerebellar Nuclei 70
9. Conclusions 72
References 73

I. List of Abbreviations

^{1}H	-	hydrogen (Proton)
^{23}Na	-	sodium
^{31}P	-	phosphorus
AE	-	alcohol exposed
AMC	-	absolute metabolite concentration
ARBD	-	alcohol-related birth defects
ARND	-	alcohol-related neurodevelopmental disorders
bw	-	brain water
Ca^{2+}	-	calcium ion
CC	-	corpus callosum
CHESS	-	chemical shift selective
Cho	-	choline
CNS	-	central nervous system
COMAC-BME	-	Biomedical Engineering Concerted Actions' Committee
Cr	-	creatine
CRLB	-	Cramér-Rao lower bounds
CS	-	Conditioned stimulus
CSF	-	cerebrospinal fluid
CUBIC	-	Cape Universities Brain Imaging Centre
CVLT	-	California Verbal Learning Test
DAG	-	diacylglycerol
DTI	-	diffusion tensor imaging
EBC	-	eye blink conditioning
EVS	-	extra volume suppression (%)
FA	-	fractional anisotropy
FAS	-	fetal alcohol syndrome
FASD	-	fetal alcohol spectrum disorder
FFT	-	fast Fourier transform
FID	-	free induction decay
FWHM	-	full width at half maximum (ppm)
Gd-DTPA	-	gadolinium diethyl-triamine-penta-aceticacid
Gln	-	glutamine
Glu	-	glutamate
gm	-	gray matter
GPC	-	glycerophosphorylcholine
Gx	-	magnetic gradient in x-direction
Gy	-	magnetic gradient in y-direction

Gz	-	magnetic gradient in z-direction
HE	-	heavily exposed
Hz	-	herts (per second)
IoM	-	Institute of medicine
IP_3	-	inositol 1,4,5-trisphosphate
K^+	-	potassium ion
mI	-	myo-Inositol
mm	-	millimeter
mM	-	millimoles per liter, concentration
$MnCl_2$	-	manganese chloride
MR	-	magnetic resonance
MRI	-	magnetic resonance imaging
MRS	-	magnetic resonance spectroscopy
ms	-	millisecond
Na^+	-	sodium ion
NAA	-	N-acetyl aspartate
NAAG	-	N-acetyl aspartyl glutamate
NaCl	-	sodium chloride (salt)
ND	-	neurobehavioral disorder
NMR	-	nuclear magnetic resonance
PCh	-	phosphorylcholine
PCr	-	phosphocreatine
PDMS	-	polydimethylsiloxane
PFAS	-	partial fetal alcohol syndrome
PI	-	phosphoinositide
PIP_2	-	phosphatidyl-inositol-(4,5) biphosphate
PLC	-	phospholipase C
ppm	-	parts per million
PRESS	-	point resolved spectroscopy
PVC	-	partial volume correction
RF	-	radiofrequency
ROI	-	region of interest
SE	-	selection efficiency (%)
SE	-	static encephalopathy
SI	-	signal intensity
SNR	-	signal-to-noise ratio
STEAM	-	stimulated echo acquisition mode
tCho	-	total choline
TE	-	echo time
TM	-	mixing time

TMS	-	tetramethylsilane
TR	-	repetition time of pulse sequence
US	-	unconditioned stimulus
VOI	-	volume of interest
wm	-	white matter
WS	-	water suppression (%)

II. List of symbols

A	-	unlocalised SI from metabolite in phantom's cube
B	-	unlocalised SI from metabolite in the phantom's sphere
B_0	-	main magnetic field
B_e	-	magnetic field created by electron flow
B_{eff}	-	effective magnetic field experience by spin
C	-	localised SI from metabolite in the phantom's cube
C_A	-	carbon atom A
C_{av}	-	factor accounting for the number of averages
C_B	-	carbon atom B
C_{gain}	-	adjustment according to the receiver gain settings
CH	-	methine functional group
CH_2	-	methene functional group
CH_3	-	methyl functional group
$C_{LCModel}$	-	NAA concentration in 'institutional units'
C_n	-	factor that accounts for the number of equivalent protons
C_{true}	-	actual NAA concentration in phantom
D	-	localised SI from metabolite in the phantom's sphere
d_c	-	diameter of phantom cube
F	-	calibration factor
f_C	-	number of protons in metabolite from cube
f_{csf}	-	fraction cerebrospinal fluid
f_D	-	number of protons in metabolite from sphere
f_{gm}	-	fraction grey matter
f_{wm}	-	fraction white matter
G	-	magnetic gradient
H_A	-	proton attached to carbon atom A
H_B	-	proton attached to carbon atom B

J	-	coupling constant
k	-	Boltzmann constant
$[m]$	-	actual concentration of the specific metabolite
n_α	-	the number of spins in the lower energy state
n_β	-	the number of spins in the higher energy state
$[r]$	-	actual concentration of the reference metabolite
Sbw	-	signal intensity of water in brain tissue
$Scsf$	-	signal intensity of cerebrospinal fluid
S_m	-	adjusted metabolite signal intensity
S_r	-	adjusted reference metabolite signal intensity
T	-	absolute temperature in Kelvin
T_1	-	longitudinal relaxation time
T_2	-	transverse relaxation time
W_{conc}	-	water concentration in mM units
W_{sup}	-	suppressed water signal
W_{unsup}	-	unsuppressed water signal
α-*state*	-	protons aligned with B0 field
B-state	-	proton opposing B0 field
γ	-	gyromagnetic ratio
δ	-	chemical shift (ppm)
δ_c	-	chemical shift of substance in cube
δ_s	-	chemical shift of substance in sphere
ΔE	-	the energy difference between the high and low energy states
$\hbar$	-	Planck's constant divided by 2π
μ_e	-	magnetic moment created by electron flow
ω	-	precessional frequency
ω_0	-	Larmor frequency.
ω_{eff}	-	effective precessional frequency
ω_{ref}	-	precessional frequency of reference substance

III. List of Figures

Figure 2.1: Energy states for a spin ½ nucleus such as hydrogen 3

Figure 2.2: Opposing magnetic field (B_e) generated by electron flow 4

Figure 2.3: Vicinal carbon atoms in (a) α-α and (b) α-β spin states 6

Figure 2.4: Diagram showing the Creation of the Different Magnetic Moments (μ_e) caused by Electron Flow in the (a) α-α and (b) α-β spin states 6

Figure 2.5: Spin-Spin Splitting Pattern for Vicinal Protons 7

Figure 2.6: Pascal's Triangle 8

Figure 2.7: Typical Chemical Shift Spectrum for Brain Tissue [7] 8

Figure 2.8: Chemical Structure of (a) NAA, (b) choline, (c) myo-inositol, (d) creatine, (e) glutamate and (f) glutamine 10

Figure 3.1: PRESS pulse sequence diagram 13

Figure 3.2: STEAM pulse sequence diagram 14

Figure 3.3: A single CHESS element consisting of a frequency selective 90^o excitation followed by a magnetic crusher gradient 15

Figure 3.4: 2-Dimensional VOI Profile 16

Figure 4.1: LCModel One-Page Output [10] 18

Figure 5.1: Diagram of spectroscopic phantom 20

Figure 5.2: Experimental setup and expected spectra for (a) unlocalised experiment and (b) localised experiment with the ROI < d_c and (c) ROI > d_c 23

Figure 5.3: Model showing the compartments of the human brain as proposed by Ernst et al [13] 26

Figure 5.4: Screenshot of the CUBIC's user interface during localisation experiments 28

Figure 5.5: Screenshot of Matlab frequency domain data 29

Figure 5.6: Screenshot of scanner during Phantom tests to Determine Absolute Metabolite Concentrations 30

Figure 6.1: Localisation Profile for 20 mm Cube 34

Figure 6.2: Localisation Profile for 30 mm Cube 34
Figure 6.3: Localisation Profile for 50 mm Cube 35
Figure 6.4: EVS for 20 mm Cube 36
Figure 6.5: EVS for 30 mm Cube 36
Figure 6.6: EVS for 50 mm Cube 37
Figure 6.7: Contamination for 20 mm Cube 38
Figure 6.8: Contamination for 30 mm Cube 38
Figure 6.9: Contamination for 50mm Cube 39
Figure 6.10: Water Suppression Efficiency 40
Figure 6.11: Spectra from Localisation Phantom with 20 mm Cube obtained with both automated (left) and manual (right) shimming 40
Figure 6.12: Spectra from Localisation Phantom with 30 mm Cube obtained with both automated (left) and manual (right) shimming 42
Figure 6.13: Absolute Metabolite Concentration in Phantom as Calculated by the Calibration Factor. 44
Figure 6.14: Absolute Metabolite Concentration in Second Phantom as Calculated by Water Scaling. 45
Figure 7.1: PRESS Profile for 30 mm Cube when (a) VOI = 20 mm, (b) VOI = 30 mm and (c) VOI = 40 mm. 47
Figure 8.1: Experimental Setup for EBC 58
Figure 8.2: Neural Pathways of EBC [55] 59
Figure 8.3: Conditioned Response from Session One to Session Two [61] 61
Figure 8.4: User Interface during *in vivo* MRS Data Acquisition in FASD study 65
Figure 8.5: Example of Bi-exponential curve fitting where S_{CSF}:S_{BW} is 2:3 66
Figure 8.6: Example of Bi-Exponential Curve Fitting 67
Figure 8.7: Total Myo-Inositol Concentrations in Deep Cerebellar Nuclei. 69
Figure 8.8: Mean Myo-Inositol Concentrations in Deep Cerebellar Nuclei. 69
Figure 8.9: Mean total Choline Concentrations in Deep Cerebellar Nuclei. 70

IV. List of Tables

Table 6.1: Mean FWHM and SNR values for All Localisation Phantom Cube Volumes at TE30 32

Table 6.2: Mean FWHM and SNR values for All Localisation Phantom Cube Volumes at TE135 32

Table 6.3: Mean FWHM and SNR values for All Localisation Phantom Cube Volumes at TE270 33

Table 8.1: FASD study where Eye Blink Conditioning Criteria were first Met [61] 60

Table 8.2: Subject Data after Exclusion Criteria 67

Table 8.3: Mean Results for all Metabolites Studied 68

1. Introduction

Nuclear magnetic resonance (NMR) is a technique with wide application in medical research fields. Probably the most widely known application is in magnetic resonance imaging (MRI) that was first demonstrated in the 1970's [1] and allows structures in any organism – brain, heart, muscles, etc – to be imaged and studied *in vivo*.

Magnetic resonance spectroscopy (MRS) is based on NMR principles and allows investigation of the chemical composition of certain tissues. It is only recently that MRS has become possible *in vivo* enabling a range of possible applications, such as the development of more effective and reliable drugs for treatment through a better understanding of the chemical composition of tissues associated with specific diseases, as well as non-invasive biopsies. Prior to the development of this technology, chemical composition of many tissues in the human body could only be determined post-mortem and therefore could not aid in the detection and diagnosis of disease.

The nuclei that are most commonly studied with MRS include hydrogen (^{1}H), sodium (^{23}Na), and phosphorus (^{31}P). In this study only hydrogen (^{1}H) spectroscopy, also called proton spectroscopy, was used. As such, spectra give information of the relative concentrations of the different metabolites containing hydrogen in a selected volume of interest (VOI). Studies of the respective cerebral metabolites have suggested correlations between their concentrations and certain pathologies, so even though their functions are not completely understood, trends could point to specific diagnoses.

One metabolite concentration that seemed to be resistant to change is creatine (Cr), which was found to remain essentially constant in the presence of most pathological conditions. It is for this reason that spectroscopic results were historically expressed as ratios to creatine. Although this assumption has since been disproved [2, 3], the convention remains, often making interpretation of findings difficult as relative changes may result from changes of either the numerator or the denominator. Therefore, in order to report meaningful results, the need to determine the absolute concentrations of the cerebral metabolites in the familiar SI units of mM has emerged.

Determining absolute metabolite concentrations is not the only obstacle that has to be overcome in MRS. Many *in vivo* MRS studies of different pathological conditions have been conducted and findings are reported widely in the literature. Inter-scanner variability has, however, been a big limitation of MRS studies and it is one of the main reasons why this method has not been established as a reliable diagnostic tool [1]. Before this goal can be achieved, broad databases related to specific pathological conditions must be created, but the inconsistent results found between different scanners hampers the creation of such records. Many studies have been devoted to normalise the differences between scanners in order to make MRS data more reproducible and reliable [1, 4, 5, 6].

The main aims of this study were:

(1) to design and build a phantom suitable for MRS studies,

(2) to perform phantom studies with known chemical substances in separate chambers to assess the accuracy of the spectra and localisation on the 3T Siemens Allegra (Siemens Medical Systems, Erlangen, Germany), scanner at the Cape Universities Brain Imaging Centre (CUBIC),

(3) to develop protocols and algorithms for the measurement of absolute metabolite concentrations, and

(4) to apply the methods developed in (3) to assess the integrity of the cerebellar deep nuclei in children with Fetal Alcohol Spectrum Disorder (FASD).

2. MRS Principles

2.1 General

Nuclear magnetic resonance (NMR) spectroscopy or magnetic resonance spectroscopy (MRS) is an analytical method to determine the chemical composition of a substance *in vitro* or of tissues *in vivo*. This proposal will only highlight aspects of MRS not usually covered in the study of MRI.

2.2 Precession of Spins

As in MRI, when hydrogen nuclei are placed in a large magnetic field, B_0, they precess with their spins aligned either parallel or anti-parallel to B_0, which is typically denoted by the z-axis. Spins precessing parallel to B_0 are at a lower energy state (α-state) than spins opposing the main magnetic field (β-state). The energy diagram is shown in figure 2.1.

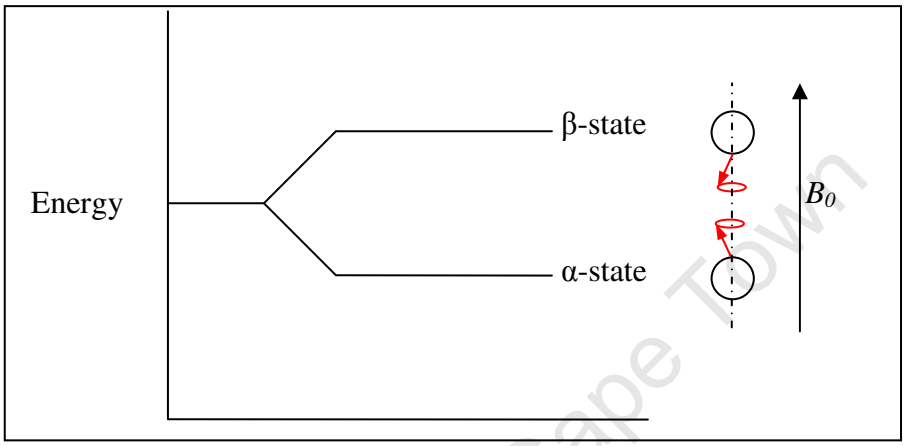

Figure 2.1: Energy states for a spin ½ nucleus such as hydrogen.

There is a small temperature-dependent excess of spins in the lower (α) energy state given by the Boltzmann equation [7]

$$\frac{n_\alpha}{n_\beta} = e^{\Delta E/kT} = e^{\hbar\omega/kT} \quad , \qquad \text{(Eq 2.1)}$$

where

n_α is the number of spins in the lower energy state

n_β is the number of spins in the higher energy state

ΔE is the energy difference between the two states

k is the Boltzmann constant

T is the absolute temperature in Kelvin

$\hbar$ is Planck's constant divided by 2π

ω is the Larmor frequency.

After applying an rf (radiofrequency) pulse, this equilibrium is disturbed and it is the return of the excess spins to the α-state that induces an emf in the scanner's receiver coil and gives rise to the MRI signal, termed a free induction decay (FID). The longitudinal and transverse relaxation time constants, T_1 and T_2 respectively, describe the time that elapses before the spin system returns to a steady state arrangement again.

2.3 Chemical Shielding and Chemical Shift

Chemical shielding forms the basis of MRS. According to the atom model as presented by Bohr, all protons are surrounded by electrons and the motion of these charges create a magnetic moment (μ_e) opposing the main magnetic field (figure 2.2) [7]. This magnetic moment is so small that it is neglected in typical MRI studies, but in MRS the resulting field relays critical information regarding the chemical environment of the protons.

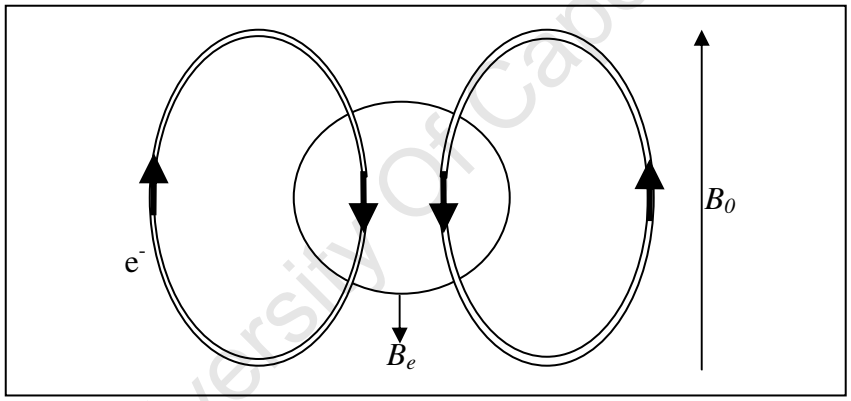

Figure 2.2: Opposing magnetic field (B_e) generated by electron flow

The effective local magnetic field experienced by all protons is therefore not equal to B_0, but to the difference between the two resulting magnetic fields

$$B_{eff} = B_0 - B_e \ . \qquad \text{(Eq 2.2)}$$

The effective magnetic field is therefore directly related to the local chemical environment of the proton being studied and according to the Larmor equation, the rate of precession will change with the effective magnetic field (B_{eff}) and is given by

$$\omega_{eff} = \gamma B_{eff}\,, \qquad \text{(Eq 2.3)}$$

in which γ is the gyromagnetic ratio.

In order to normalise the effect of different B_0 field strengths, chemical shift (δ) is defined as the relative increase or decrease of the precessional frequency of a proton (ω_{eff}) compared to that of a proton in a reference substance (ω_{ref}) and is given by

$$\delta = \frac{\omega_{eff} - \omega_{ref}}{\omega_{ref}}\,. \qquad \text{(Eq 2.4)}$$

In vivo MRS usually uses water as reference. As mentioned before, the change in precessional frequency is very small – typically a few Hertz (Hz), while precessional frequencies are of the order of tens of MHz for magnetic field strengths typically used in MR scanners. For this reason, chemical shift is reported in the dimensionless units parts per million (ppm).

Protons in different chemical environments will resonate at different frequencies, i.e. have different chemical shifts. For molecules containing more than one proton in dissimilar chemical environments, the spectra will contain multiple peaks representing the respective proton types.

2.4 Spin Configurations and Spin-Spin Splitting [8]

As seen in the previous section, very small forces, such as electron flow in chemical shielding, affects the chemical shift of a proton. Different protons in the same molecule will also have a magnetic effect on each other. This is a phenomenon referred to as spin-spin splitting.

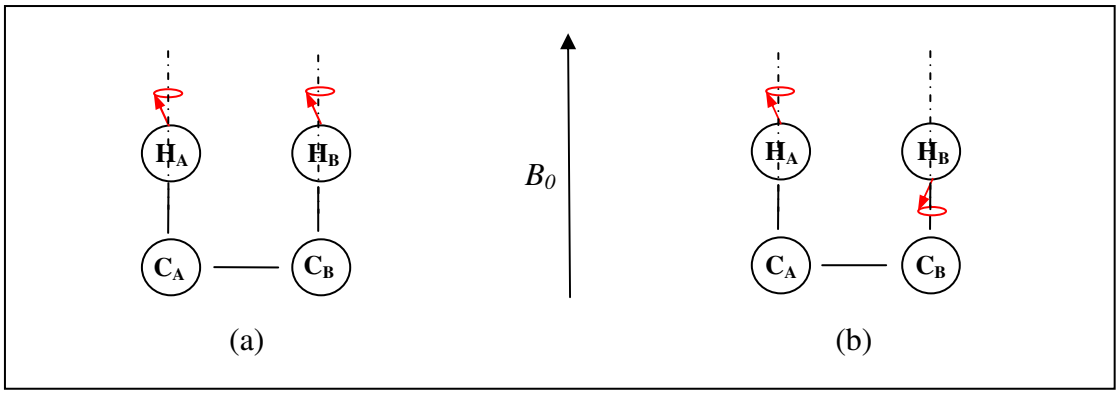

Figure 2.3: Vicinal carbon atoms in (a) α-α and (b) α-β spin states

Figure 2.3 shows two identical molecules with both protons in the α-state in (a) and proton A in the α-state and proton B in the β-state in (b). Figure 2.4 illustrates the effect of spin coupling.

Figure 2.4: Diagram showing the Creation of the Different Magnetic Moments (μ_e) (Blue Arrows) caused by Electron Flow in the (a) α-α and (b) α-β spin states

In figure 2.4(a) the electrons surrounding the two protons move in a similar fashion due to the α-α configuration and the electrons essentially form an 'electron cloud'. This means that electrons are allowed to move farther away from the nucleus and therefore leads to less effective shielding of the protons, i.e. smaller B_e. The opposing configuration in 2.4(b) forces the electrons to move closer to their respective nuclei, resulting in greater shielding of the proton. This results in:

- Smaller B_e and a larger B_{eff} for the α-α state
- Larger B_e and a smaller B_{eff} for the α-β state

- The effective magnetic field experienced by protons in the α-α configuration is larger than it would have been in the absence of a second proton
- The effective magnetic field experienced by protons in the α-β configuration is smaller than it would have been in the absence of a second proton

From the Larmor equation, this translates to the fact that protons in the α-α configuration would have higher resonance frequencies than the protons in the α-β configuration. In turn, protons in the α-α and the α-β-states will precess at respectively higher and lower frequencies than a lone proton (figure 2.5).

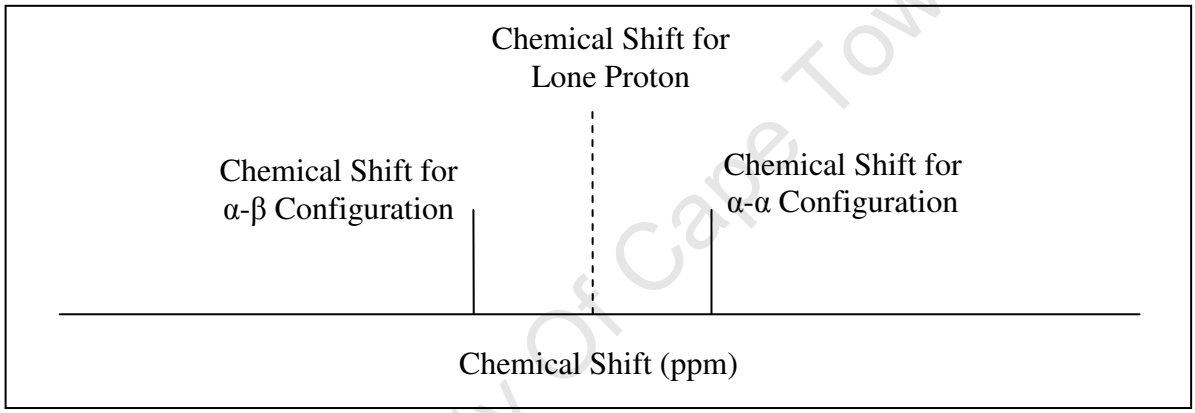

Figure 2.5: Spin-Spin Splitting Pattern for Vicinal Protons

As the complexity of the molecule increases, so does the complexity of the spectrum and this leads to a principle called spin-spin splitting. The n+1 rule predicts the number of distinct peaks that would occur in a spectrum for *n* chemically equivalent protons by taking into account all possible spin configurations in a molecule.

As the complexity of the molecules increase, Pascal's triangle (figure 2.6) can be used to predict the shapes and heights of the peaks surrounding the original chemical shift.

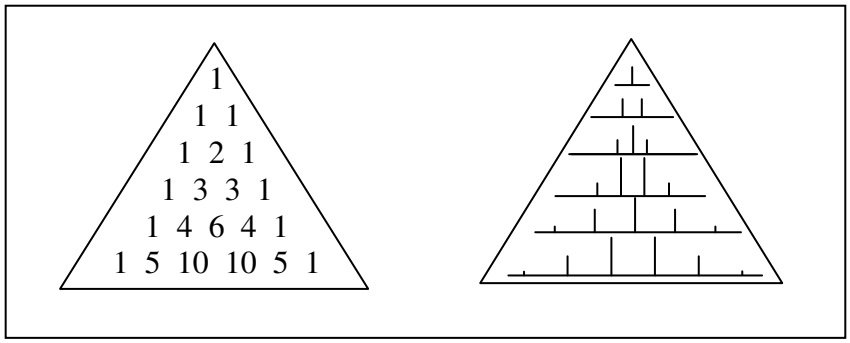

Figure 2.6: Pascal's Triangle

Finally, the distance (in ppm) between each of the peaks is given by the coupling constant denoted by the symbol *J*. The value of this constant is specific for interactions between various protons which means that the effect that a certain proton has on a vicinal proton, is always the same. The effects that protons have on each other are neglected when more than three bonds separate the protons, as their interaction is very small.

2.5 Cerebral Metabolites of Interest in MRS [7]

The spectrum obtained from *in vivo* proton MRS of the human brain is shown in figure 2.7 below. The chemical shift in ppm is plotted on the x-axis, while the y-axis represents quantitative data regarding each of the metabolites. The area under a specific metabolite peak corresponds to the concentration of that metabolite in the volume of interest.

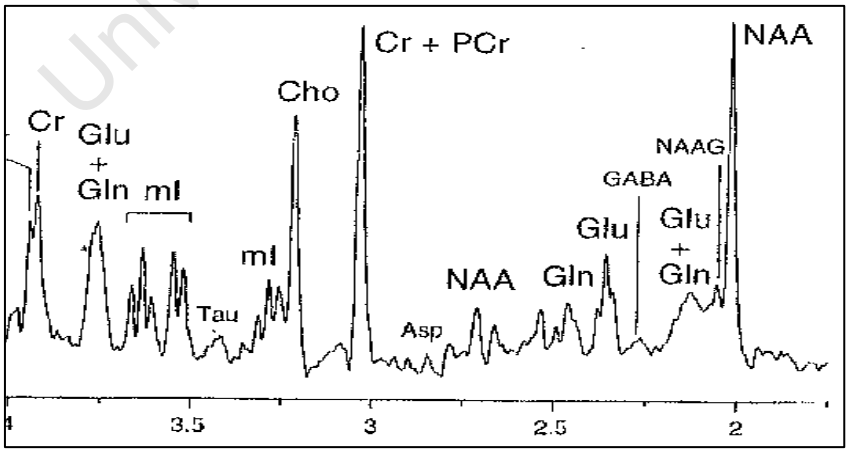

Figure 2.7: Typical Chemical Shift Spectrum for Brain Tissue [7]

Most cerebral metabolites contain protons and therefore there is quite a wide range of metabolites that are of importance in proton spectroscopy. It is, however, not within the scope of this project to study the metabolites' exact role in the brain's metabolic activities and therefore only a short description of a few of the most prominent metabolites will be given in this section.

NAA: N-acetyl aspartate is a cerebral metabolite with a very prominent singlet resonance at 2.008 ppm created by the methyl (CH_3) group in the molecule's structure. The proton in the methine (CH) group creates a multiplet at 4.382 ppm, while the protons in two methene (CH_2) groups form double doublets at 2.486 and 2.673 ppm respectively. A single amide proton is evident at a chemical shift of 7.28 ppm. NAA is found solely in the central and peripheral nervous system and is often used as a marker of neuronal density. It has, however, been noticed that NAA concentrations also decrease in pathologies where neuronal dysfunction is encountered. Therefore NAA is most frequently used a marker of neuronal integrity.

NAAG: N-acetyl aspartyl glutamate is a neurotransmitter with a singlet resonance at 2.042 ppm created by a methyl group, as well as three double doublets at 2.519, 2.721 and 4.607 ppm from two methene groups and one methine group respectively. The additional glutamate moleculte added to the standard NAA molecule adds several more peaks to the spectroscopic data – a double doublet at 4.128 from a methine group and four multiplets at 1.881, 2.049, 2.190 and 2.180 from methene groups. The strong overlap between NAA and NAAG's resonances makes it very difficult to resolve the spectra from these two compounds. Therefore NAA concentrations are often given as the sum of NAA and NAAG as these results are more reliable.

Choline: A prominent singlet resonance is found at 3.185 ppm from choline-containing compounds which is formed by three methyl groups. Two multiplets, created by two methene groups are also encountered at chemical shifts of 3.501 and 4.054 ppm. Free choline only accounts for a very small fraction of the total choline concentration *in vivo* as most of it is made up of glycerophosphorylcholine (GPC) and phosphorylcholine

(PCh). It has been found that the concentration of choline increases as a function of cell membrane turnover.

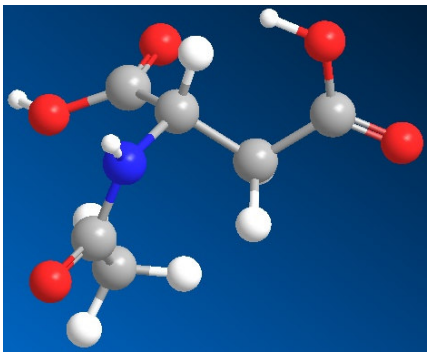

(a)

(b)

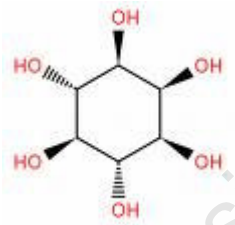

(c)

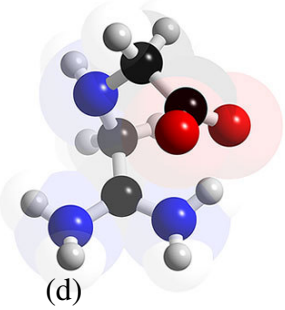

(d)

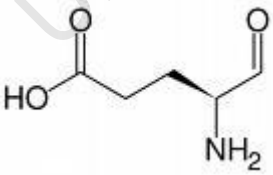

(e)

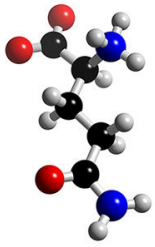

(f)

Figure 2.8: Chemical Structure of (a) NAA, (b) choline, (c) myo-inositol, (d) creatine, (e) glutamate and (f) glutamine

Myo-Inositol: Myo-inositol is a chemical compound with six NMR resonances – all consisting of double doublets and created by protons in methine groups – two at 3.522 ppm, one at 3.269 ppm, one at 4.054 ppm and two at 3.614 ppm. mI has been found to be an important osmolyte, as well as being involved in the phosphoinositide signal transduction pathway. It has also been theorised that mI is a marker of supporting glial cells.

Creatine: It has been shown that creatine (Cr) and phosphocreatine (PCr) play a vital role in the energy metabolism of cells. Pure creatine has three singlet resonances at 3.027, 3.913 and 6.650 created by a methyl, methene and amide group respectively. The similarity between the Cr and PCr resonances also lead to the total creatine reported being the sum of the free Cr and PCr.

Glutamate: Glu is found in all cell types and has several functions ranging from being a neurotransmitter to the synthesis of other metabolites. A double doublet resonance created by a methine group is observed at 3.746 ppm as well as four multiplets at 2.120, 2.042, 2.336 and 2.352 ppm respectively formed by four methene groups.

Glutamine: Gln is located mostly in the astroglia and is formed from Glu. The primary function of Gln is the detoxification of ammonia. Increased Gln levels in the brain are therefore a marker to determine whether the patient suffers from hepatic encephalopathy. The chemical shift of Gln protons creates a double doublet at 3.757 ppm (CH) and four multiplets at 2.135, 2.115, 2.434 and 2.456 ppm (CH_2). The close proximity between the Glu and Gln resonance make the very difficult to resolve, however it is possible when using field strengths exceeding 7 Tesla.

3. MRS Pulse Sequences

The most pronounced difference between a MRI and MRS sequence is the absence of a readout gradient during data acquisition in MRS. MRS is challenging due to the fact that very sensitive metabolite data must be obtained in a localized volume of interest (VOI). The sequences therefore need to destroy unwanted spin coherences outside the VOI

without compromising data acquisition of the metabolite signals within. The two main sequences that are used for single voxel spectroscopy are STEAM and PRESS.

3.1 Point Resolved Spectroscopy (PRESS)

PRESS is a sequence that has gained popularity among the spectroscopy community due to the fact that the metabolite signal obtained is twice the magnitude of that acquired with STEAM.

The PRESS sequence consists of a 90^o slice selective excitation pulse followed by two slice selective, refocusing 180^o pulses. The slice selective gradients for these three pulses are applied in three mutually orthogonal directions. This sequence gives rise to three signals, the first being the free induction decay (FID) from the 90^o excitation, which contains signal from all spins in the slice selected with this pulse. The first spin echo is generated by the first 180^o pulse and contains signal from spins located along the column where the two orthogonal slices selected by the first two pulses intersect (figure 3.1c). The final spin echo - and the signal of interest - follows after the last 180^o pulse and at time TE after the initial excitation. The signal for this echo is the summation of all the slice selections and emanates from the voxel where the slice selected by the last 180^o pulse intersects the column formed by the previous two pulses.

The timing of the pulse sequence is shown in figure 3.1. After the initial excitation pulse a quarter of the total echo time lapses before the first 180^o pulse is performed. Following this pulse, a time TE/2 passes until the second 180^o pulse is performed. The second spin echo (SE2) is formed at time TE after the initial excitation.

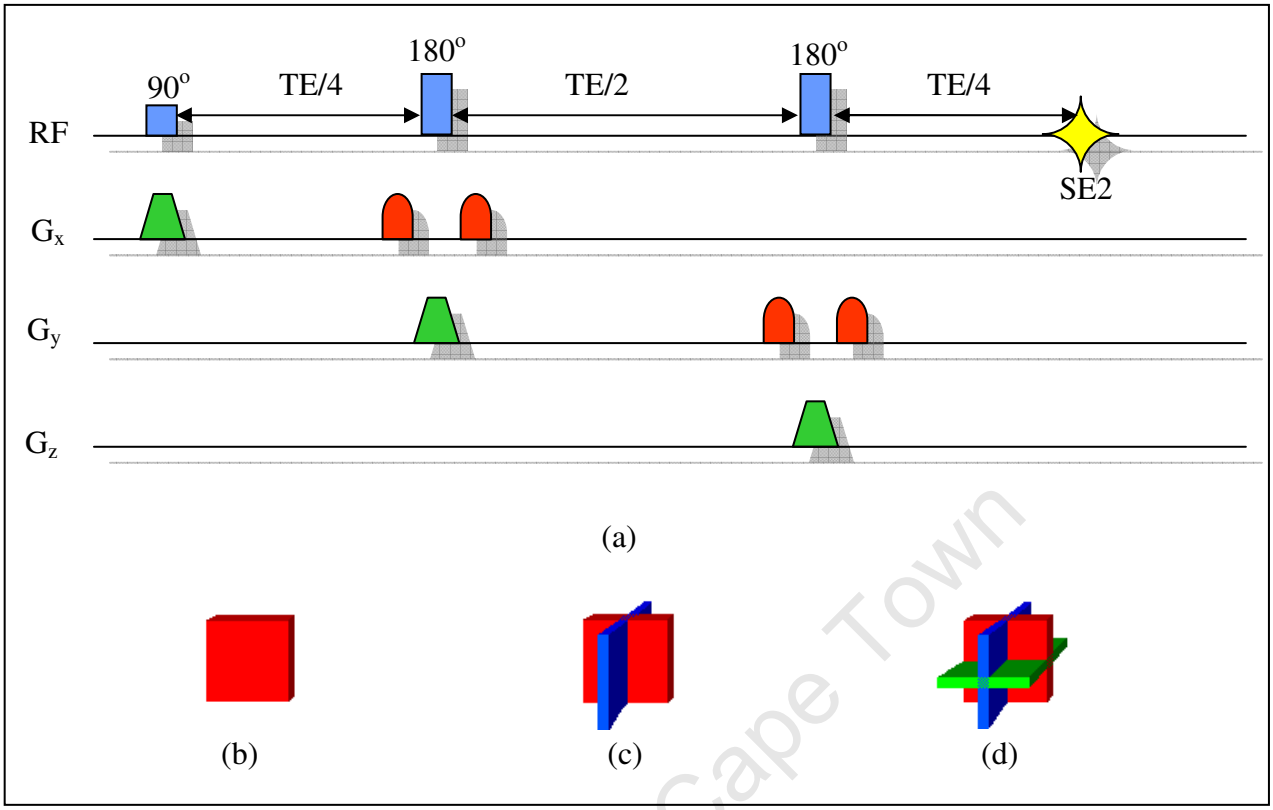

Figure 3.1: (a) PRESS pulse sequence (b) The first FID signal results from spins located in the slice selected by the 90° excitation pulse (c) Spins located in the columnar volume where the two orthogonal slices intersect give rise to the signal in the first spin echo (SE1) (d) The final spin echo (SE2) consists of the signal from spins located in the cubic volume where all three selected slices intersect. This is the only signal desired from the pulse sequence.

As illustrated in figure 3.1, crusher gradient pairs surround both the 180° pulses in order to destroy remaining transverse magnetization outside the region of interest resulting from the initial FID and the first spin echo (SE1).

3.2 Stimulated Echo Acquisition Mode (STEAM)

The STEAM sequence consists of three 90° frequency selective pulses with the slice selective gradients applied in three mutually orthogonal directions. Three simple FID's and four spin echoes are formed by this sequence, but the only signal of interest is a stimulated echo (STE) formed after the total echo and mixing time (TE +TM) has elapsed. Crusher gradients are applied to eliminate all signal from the spin echoes and FID's, leaving only the stimulated echo to be acquired. Only spins that experienced all

three 90 degree pulses will contribute to the final signal, and these spins will be localised in a cubic volume where the three slice selective gradients intersect.

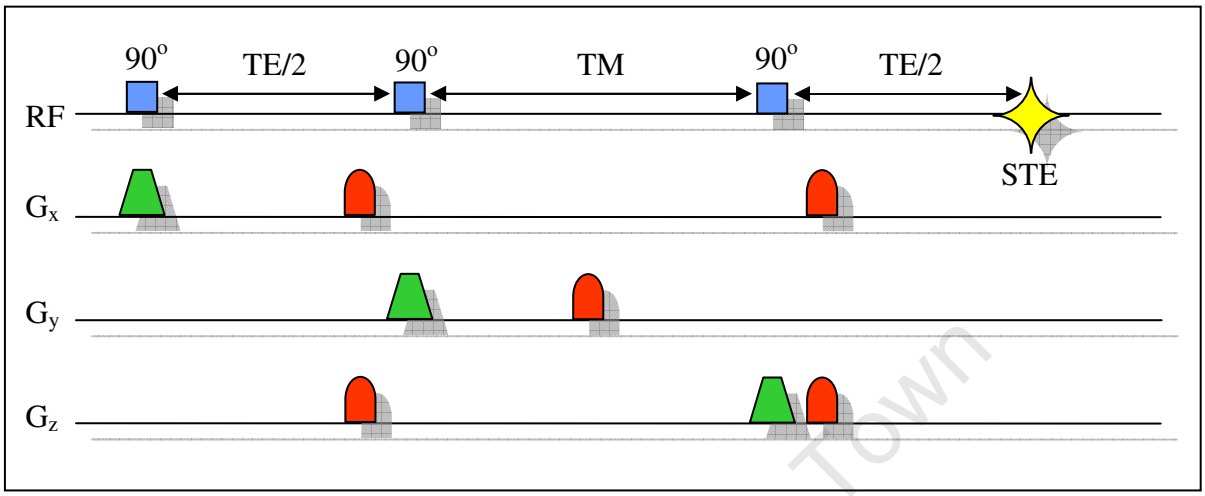

Figure 3.2: STEAM pulse sequence diagram

The main advantage of the STEAM sequence is better localisation due to the use of 90° pulses only compared to the 90°-180°-180° sequence used in PRESS. The main disadvantage of the STEAM sequence is the fact that stimulated echoes typically have a 50% reduction in signal amplitude, rendering a significantly lower SNR when compared to the PRESS sequence.

3.3 Water Suppression

The human brain contains approximately 77% water by mass at concentrations of up to 55.56 M whereas the metabolites being studied are typically found in the concentration range from 7 to 15 mM. The overpowering water resonance at around 4.7 ppm therefore clearly needs to be greatly reduced, if not eliminated, in order to get reliable metabolite spectra. Elimination of the water signal also reduces quantification difficulties due to baseline distortion.

There are many ways to suppress the water signal, some of which are [7]:

- frequency selective techniques

- exploiting differences in relaxation parameters
- spectral editing techniques and
- software-based methods.

Siemens scanners employ a CHEmical Shift Selective (CHESS) water suppression technique.

A CHESS sequence employs frequency selective RF pulses to excite the water spins into the transverse plane, after which a magnetic gradient is applied to destroy all phase coherences between the spins. This means that immediately after the water suppression sequence has been applied, there is no net water signal and there should be no more water spins aligned with the B_0 field that could be excited. It is only after the CHESS sequence has been applied that the metabolites are excited by the chosen pulse sequence. The frequency selective RF pulse leaves the spins belonging to metabolites with resonances outside the range of water completely undisturbed. This is one of the great advantages of this method of water suppression.

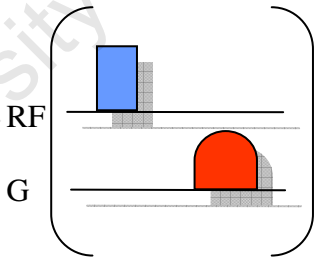

Figure 3.3: A single CHESS element consisting of a frequency selective 90^o excitation followed by a magnetic crusher gradient

Ideally a single CHESS element (figure 3.3) should be sufficient to suppress the entire water signal in a voxel, but unavoidable B_0 inhomogeneities necessitate the use of multiple CHESS elements for water suppression. Scanners employing CHESS sequences typically use three CHESS elements prior to metabolite excitation. With regard to water suppression, the STEAM sequence has a distinct advantage over the PRESS sequence as more CHESS elements can be applied during the TM period, leading to better water

suppression. This altered STEAM sequence is more commonly referred to as DRYSTEAM.

3.4 Signal Losses and Contamination

The scanner interface allows the user to select the location and size of the VOI on an MRI image of the object being scanned. The VOI is typically a cube, but different shapes can also be set. It is, however, impossible to select the perfect volume as specified by the user due to system inhomogeneities. All MR scanners using localisation sequences therefore have a distinct VOI profile associated with the specific localization sequence that allows nominal errors to account for these inconsistencies.

A typical VOI profile will extract the maximum signal from the VOI at a volume slightly smaller than the selected VOI and will then drop off linearly to zero at a position outside the VOI [9]. This leads to (1) signal loss from the VOI and (2) contamination from the out of voxel region. Figure 3.4 shows three different sources of error related to the signal obtained with PRESS and STEAM localization. The solid line represents the VOI selected by the user, while the dotted line is the actual volume selected by the scanner.

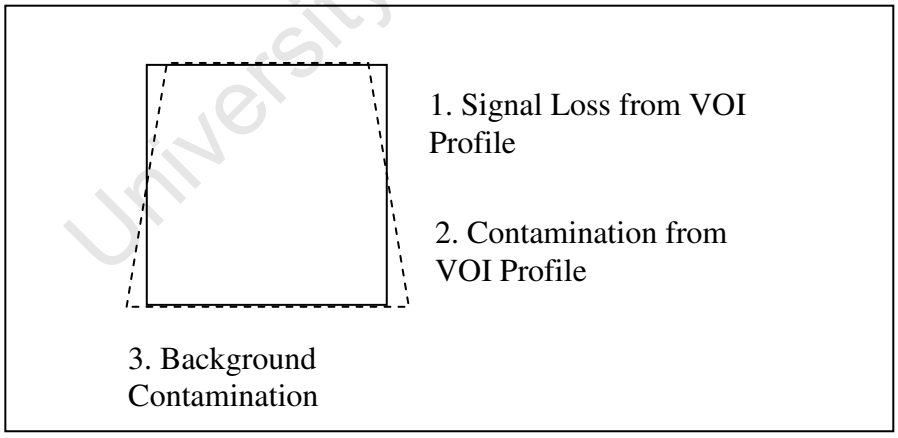

Figure 3.4: 2-Dimensional VOI Profile

Another type of contamination, usually called background contamination (3), is encountered when signal from the previously excited slices distorts the spectra. In PRESS and STEAM sequences, this type of contamination is very effectively eliminated

by spoiler gradients. It is therefore safe to say that profile contamination (ie. 1 and 2 in figure 3.4) contributes most to the total contamination encountered in these spectra. Since the PRESS pulse sequence is used in this study, the VOI profile will be referred to as the PRESS profile from hereon.

4. Linear Combination Modelling and LCModel

LCModel is Fortran-based software used to analyse raw *in vivo* spectroscopy data by means of linear combination modelling algorithms [7, 10]. Linear combination modelling of NMR spectra is based on the fact that the complete spectrum of a heterogeneous chemical system consists of a linear combination of the respective isolated components it is made up of.

The spectra of the isolated components are known as the basis spectra and it is vital that the basis sets for all possible *in vivo* metabolites are available. The software fits these basis sets to the spectral peaks of the obtained data to determine the ratios of the various metabolites in the volume of interest. Linear combination modelling therefore makes use of prior knowledge.

Determining these basis sets through *in vitro* experiments would be very time consuming and subject to experimental error. It is for this reason that the various basis sets at all echo times and employing different pulse sequences are usually simulated in programs like GAMMA and QUEST [7].

LCModel renders results as ratios to creatine, as is done by most spectroscopic data, as well as in absolute concentrations. These absolute concentrations are, however, not in the familiar SI units of mM, but rather in 'institutional units'. This simply means that for all studies performed on a specific scanner, the results can be compared as absolute concentrations. This feature becomes worthless, though, when comparing studies performed on different scanners due to inter-scanner variability [10].

The reliability of LCModel's results is indicated by the Cramér-Rao lower bounds (CRLB). The LCModel manual recommends that any results with CRLB's greater than 20% should be discarded, whilst any data with errors below this value should be reliable. Other sources [7] suggest that CRLB's between 20 and 30 % should be treated with caution.

LCModel also applies curve fitting to account for chemical shift artefacts. The fitting is done according to three landmark metabolites in the human brain: NAA (2.01 ppm), creatine (3.03 ppm) and choline (3.22 ppm).

The typical output from LCmodel is shown in figure 4.1:

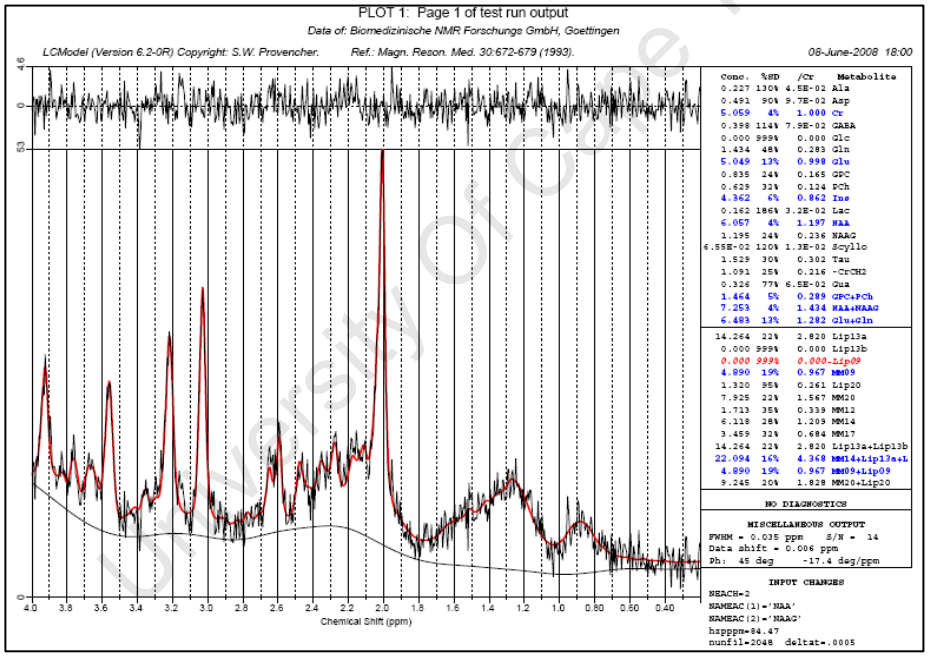

Figure 4.1: LCModel One-Page Output [10]

In figure 4.1 the black spectrum in the main chart area is the real frequency domain data and the red curve represents the LCModel fit to the data. The smooth black line at the bottom of the plot is the baseline. The baseline should follow the real data and any inconsistent trends in the baseline could point to the presence of artefacts, the presence of

alien substances or incomplete water suppression. All analyses with wild baselines should be discarded as the results obtained for these analyses are most likely inaccurate.

The erratic black line at the top represents the residuals i.e. the LCModel fit subtracted from the real data. The residuals should not have any distinct peaks or valleys and must be completely random.

The LCmodel software can also be applied for spectroscopy of muscle-, liver- and breast tissue.

5. Methods

5.1 Localisation Phantom

Phantom studies are generally used to create optimal conditions for studying certain physical systems. It is therefore crucial to use measurement parameters that reinforce these settings. It is with this in mind that a phantom was designed and built based on the specifications given in the COMAC-BME study [5]. This paper recommends that the phantom should be constructed as follows:

- An inner cube constructed from 3 mm Perspex with an inner diameter of 50 mm (figure 5.1).
- An outer sphere constructed of 5 mm Perspex with an inner diameter of 150 mm. A circular opening with 80 mm diameter should be positioned at the top of the sphere to allow easy entry and exit for the cube.
- A well-sealed lid and a cylindrical Perspex rod with an outside diameter of 12 mm to keep the cube in position.

In order to increase the flexibility of the experiments, two extra cubes were constructed with 4 mm Perspex. They have inner diameters of 20 and 30 mm respectively.

In order to obtain optimal spectral data from the phantom studies, the substances filling the phantom should comply with certain requirements:

- The spectra of the chemicals should consist of singlets
- The solutions have to be inert to reactions with the Perspex and for general safety it should not be combustible
- The chemical shift between the two liquids should be large enough to eliminate overlap, but small enough to greatly reduce or eliminate chemical shift artefacts during localisation
- Since spin echoes are mostly employed in proton MRS, it is desirable that both the liquids have the same or similar T_2 values

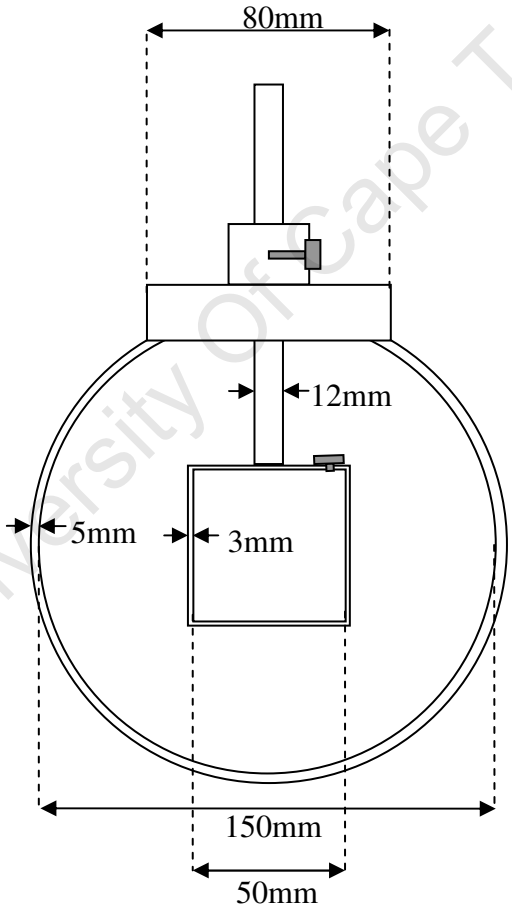

Figure 5.1: Diagram of spectroscopic phantom

The original study [5] used polydimethylsiloxane (PDMS) with singlet resonances at 0.21 and 0.14 ppm with respect to tetramethylsilane (TMS) for the inner cube and an aqueous solution of 0.1 mM Gd-DTPA, 0.09 mM NaCl and 0.05 mM $MnCl_2$ in the outer sphere.

For this study, however, two cerebral metabolites were used to assess the performance of the scanner since that is ultimately the purpose of the equipment.

A 50 mM aqueous solution of NAA was used in the inner cube. As mentioned in section 2.7, NAA's NMR spectrum consists of 5 resonances with a very prominent singlet resonance at 2.008 ppm from the acetyl moiety. In the outer sphere, a 100 mM aqueous solution of choline was used. As for the NAA, the singlet resonance in choline's NMR spectrum was be used. This singlet is found at a chemical shift of 3.185 ppm.

A base solution with 72 mM potassium phosphate dibasic (K_2HPO_4, Sigma-Aldrich P2222), 28 mM potassium dihydrogen-phosphate (KH_2PO_4, Aldrich 229806) and 1 g/l sodium azide (NaN_3, Sigma-Aldrich S8032) was first prepared. The K_2HPO_4/KH_2PO_4 combination forms a buffer solution similar to that found in human cerebrospinal fluid (CSF), whilst the NaN_3 is a preservative which prevents the solution from decomposing too fast.

The NAA (Fluka 00920) and choline (Sigma 26978) were, respectively, added to separate batches of this solution. Certain metabolites, especially NAA, are very sensitive to the pH of the environment and the resonances tend to shift at varying pH levels. It was therefore very important to create a mixture that has a pH similar to that of the brain by titrating the solution with either sodium hydroxide (NaOH, Sigma 72068) or hydrochloric acid (HCl, Fluka 84435) until a final pH of 7,2 was obtained.

5.2 Assessing Accuracy and Localisation

In order to assess scanner performance, the parameters proposed by Bovée et al [4] were measured. To this end, I acquired (a) an unlocalised acquisition from a simple 90^o FID

pulse experiment, and (b) a set of localised acquisitions at a range of different regions of interest (ROI's) (figure 5.2).

Selection Efficiency: Selection efficiency measures the percentage of the actual signal that is extracted from the ROI during localisation. Since metabolite concentrations *in vivo* are so low, selection efficiency values must be high enough for successful spectroscopy to be plausible. To determine this parameter, localisation was performed using a range of ROI's from $0.5d_c$ to $2d_c$, where d_c denotes the inner diameter of the cube in the phantom (figure 5.2). Unlocalised spectra were also acquired. Selection efficiency is defined as the signal intensity of the localised acquisition divided by that of the unlocalised acquisition, as shown in equation 5.1. The symbols *A* and *C* refer to the signal intensities as indicated in figure 5.2.

$$SE = \frac{C}{A} \times 100\% \ . \qquad \text{(Eq. 5.1)}$$

Extra Volume Suppression Factor: *In vivo* localisation sequences must be able to successfully eliminate all signal from the out of voxel region and the scanner's ability to do this is measured by the extra volume suppression factor (EVS). The same scans are used as to measure selection efficiency, but using the signal intensities for the chemicals in the sphere. EVS is given by [11]:

$$EVS = \left(1 - \frac{D}{B}\right) \times 100\% , \qquad \text{(Eq. 5.2)}$$

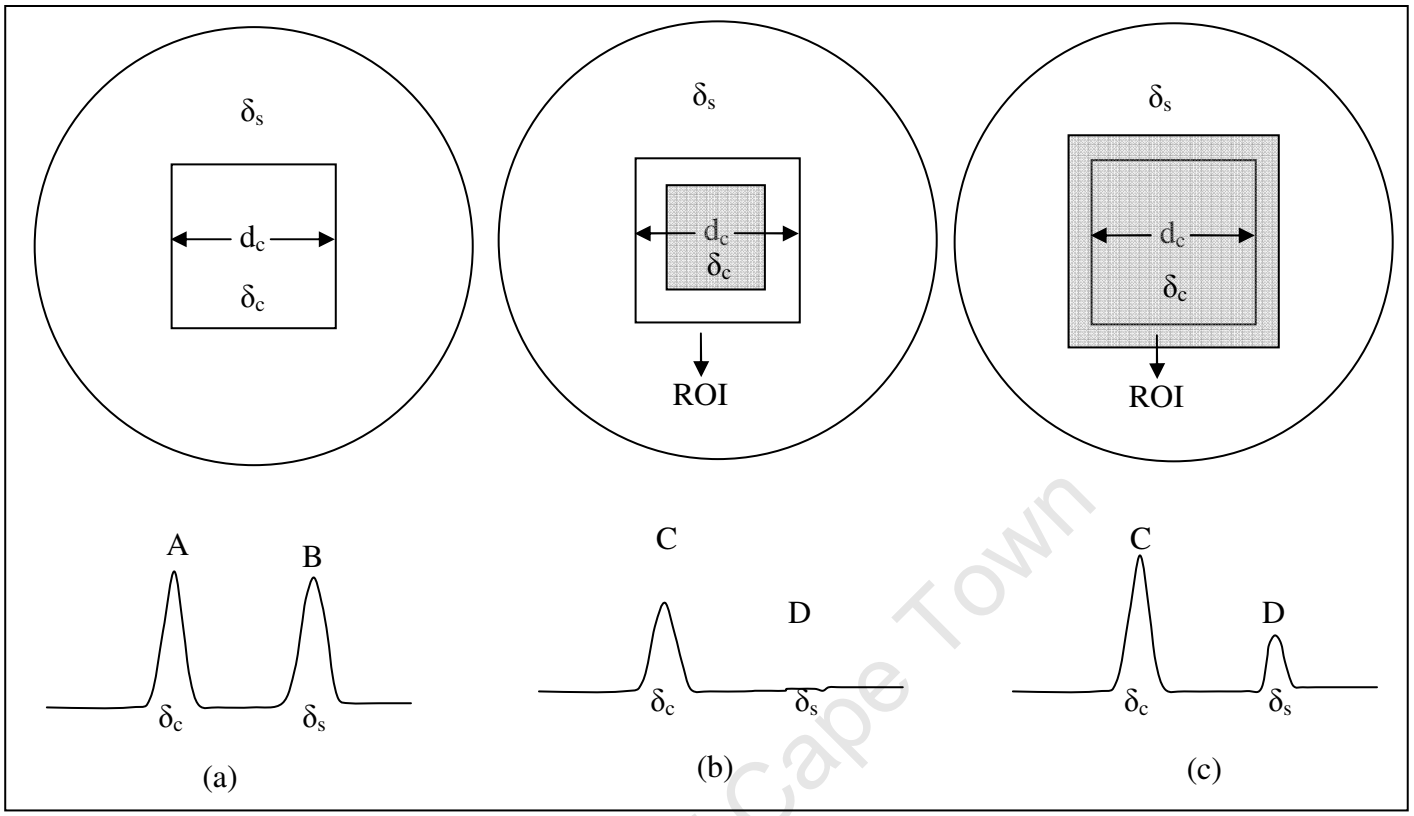

Figure 5.2: Experimental setup and expected spectra for (a) unlocalised experiment and (b) localised experiment with the ROI < d_c and (c) ROI > d_c

Contamination: This parameter measures the amount of signal from the out of voxel region, which is typically known as contamination. Contamination is influenced by the relative proton concentrations between the metabolites in- and outside the VOI and is therefore weighted by number of protons in the two different metabolites, f_D and f_C. The ROI is placed inside the cube (ROI = d_c) and the spectra are obtained. Any contribution from outside the sphere leads to contamination and is given by:

$$Contamination = \frac{f_D D}{\left(f_C C + f_D D\right)} \times 100\% . \qquad \text{(Eq. 5.3)}$$

All experiments were performed using the PRESS sequence with echo times (TE) 30 ms, 135 ms, and 270 ms, and repetition time (TR) 8000 ms, in order to ensure TR > $5T_1$ [6] to avoid saturation effects. T_1 values for NAA and choline are 1340 and 1140 ms respectively [12].

5.3 Other Performance Parameters

Effective water suppression is crucial in proton spectroscopy due to the high concentration of water in the human body, as mentioned previously. The scanner's water suppression efficiency was determined using the following equation:

$$WS = \frac{W_{un\,\mathrm{sup}} - W_{\mathrm{sup}}}{W_{un\,\mathrm{sup}}} \times 100\% \qquad \text{(Eq. 5.4)}$$

where W_{unsup} and W_{sup} are the intensities of the unsuppressed - and the suppressed water signals, respectively.

Full width at half maximum (FWHM) and SNR were also reported for all scans performed. These two parameters indicate the quality of the obtained spectra.

The last set of parameters involves the performance of the auto shimming in the scanner. Data acquired with auto shimming were compared to the same data obtained with manual shimming to determine whether the automatic shim calculation is functioning optimally.

5.4 Determination of Absolute Metabolite Concentrations

5.4.1 Calibration Factor

One way to determine absolute metabolite concentrations is to use a calibration phantom as suggested in the LCModel manual. This calibration phantom will enable the user to determine a calibration factor to convert the LCModel results given in institutional units to the more acceptable SI units of mM.

This phantom contained the same solution as that used in the inner cube of the localisation phantom:

- 50 mM NAA
- 72 mM K_2HPO_4
- 28 mM KH_2PO_4

- 1 g/L NaN_3

The calibration factor is determined by the following equation

$$F = \frac{C_{true}}{C_{LCModel}} \qquad \text{Eq. 5.5}$$

where F is the calibration factor, C_{true} is the actual metabolite concentration (50 mM NAA) and $C_{LCModel}$ is the concentration as determined by LCModel in institutional units. Scanning of the phantom and determination of the calibration factor should be done on a frequent basis to determine the stability of the scanner.

5.4.2 Water Scaling

Alternatively, absolute metabolite concentrations in a given voxel can be computed if the the actual water concentration in the VOI is known.

This is easily done in phantoms containing aqueous solutions as the concentration of water in such a solution is 55556 mM. This value can be added to LCModel's execution script and the absolute metabolite concentration will be included in the one page output.

When a heterogeneous system like the human body is scanned, the calculation becomes more complex as different tissues have different water concentrations. This problem can be resolved by using partial volume correction.

Since CSF, gray matter (gm) and white matter (wm) have different water concentrations, the fractions of each of these components in the voxel must be determined. CSF is modelled as pure water with a concentration of 55556 mM, while the water concentrations in gray and white matter are 43300 and 35880 mM, respectively [10]. The input into LCModel would then be as follows:

$$W_{conc} = f_{gm}(43300) + f_{wm}(35880) + f_{csf}(55556) \qquad \text{(Eq. 5.6)}$$

where *f* denotes the fraction of each respective component.

In order to render absolute metabolite concentrations, LCModel requires both the water suppressed and unsuppressed spectroscopic data. The cumulative signal in the unsuppressed water file is generated from only two possible compartments in the brain – the CSF and the water in the tissue of the brain. The metabolites are only found in the brain tissue and therefore neglecting to eliminate the CSF fraction would render absolute metabolite concentrations lower than they actually are.

LCModel matches the true water concentration with the integrated, unsuppressed water signal and can then scale all metabolites according to their respective integrated peaks and chemical functional groups.

5.4.3 Partial Volume Correction

Ernst et al [13] proposed the use of a compartmentalisation model to determine absolute metabolite concentrations in the brain. This model simply shows that the NMR visible part of the brain consists of CSF and the water in brain tissue (intra- and extracellular water). There is a third component which is NMR invisible and this represents the 'dry mass' of the brain, but it is not applicable to this study.

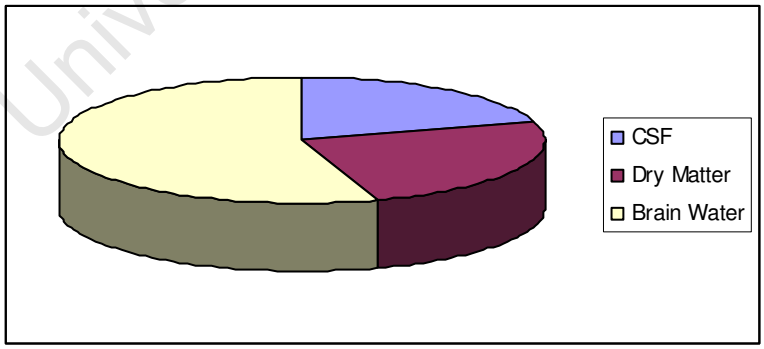

Figure 5.3: Model showing the compartments of the human brain as proposed by Ernst et al [13]

The ratio of CSF to brain water was determined by differences in the respective T_2 values. The actual signal intensity of the voxel without water suppression was

determined by scanning the voxel at a range of TE values. The signal intensity forms an exponential decay when plotted with respect to echo time.

Bi-exponential curve fitting was applied according to the signal equation for a PRESS sequence (equation 5.7) and using the T_1 and T_2 values for CSF and brain water (bw).

$$S(T_E, T_R) = S_{csf} \exp\left(\frac{-T_E}{T_{2,csf}}\right)\left[1-\exp\left(\frac{-T_R}{T_{1,csf}}\right)\right] + S_{bw} \exp\left(\frac{-T_E}{T_{2,bw}}\right)\left[1-\exp\left(\frac{-T_R}{T_{1,bw}}\right)\right] \quad \text{(Eq 5.7)}$$

The values for S_{csf} and S_{bw}, which were determined by the curve fitting procedure, represents the signal intensity for the two compartments when all relaxation effects are eliminated and therefore an accurate ratio can be determined.

Since the brain water signal consists of contributions from both gray and white matter – each with different water concentrations - it has to be processed further in order to determine the fractions of the two respective tissue types. The developer of LCModel [10] suggests either image processing or simply guessing the ratio between the two tissues as the water concentrations are fairly close.

The fraction of the brain containing the 'dry mass' can also be determined by scanning an external standard. From this, the masses and volumes of all three of the brain compartments can be determined [13], but this is not within the scope of this study.

5.5. Data Acquisition and Processing

5.5.1 Scanner Performance

Both localized and unlocalised spectra were obtained from the phantom to assess the localisation performance of the scanner. It was important that both these types of scans matched as far as possible in terms of experimental parameters. Experiments were done with all three inner cube sizes – 20 mm, 30 mm and 50 mm.

The localized experiments required that data be obtained at different VOI's with respect to the size of the inner Perspex cube. The chosen ranges are as follows:

- 20 mm Cube – 10 mm, 15 mm, 20 mm, 30 mm, 40 mm
- 30 mm Cube – 10 mm, 20 mm, 30 mm, 40 mm, 50 mm, 60 mm
- 50 mm Cube – 20 mm, 30 mm, 40 mm, 50 mm, 60 mm, 75 mm

For each of these respective VOI's, the experiment was performed at three different echo times – 30 ms, 135 ms and 270 ms, respectively. As such, 51 scans were acquired for each complete set of localized data.

The following parameters were used for all the scans:

- 1000 Hz bandwidth
- 35 Hz water suppression bandwidth
- 64 averages
- delta-ppm: -2.7 ppm
- vector size: 1024

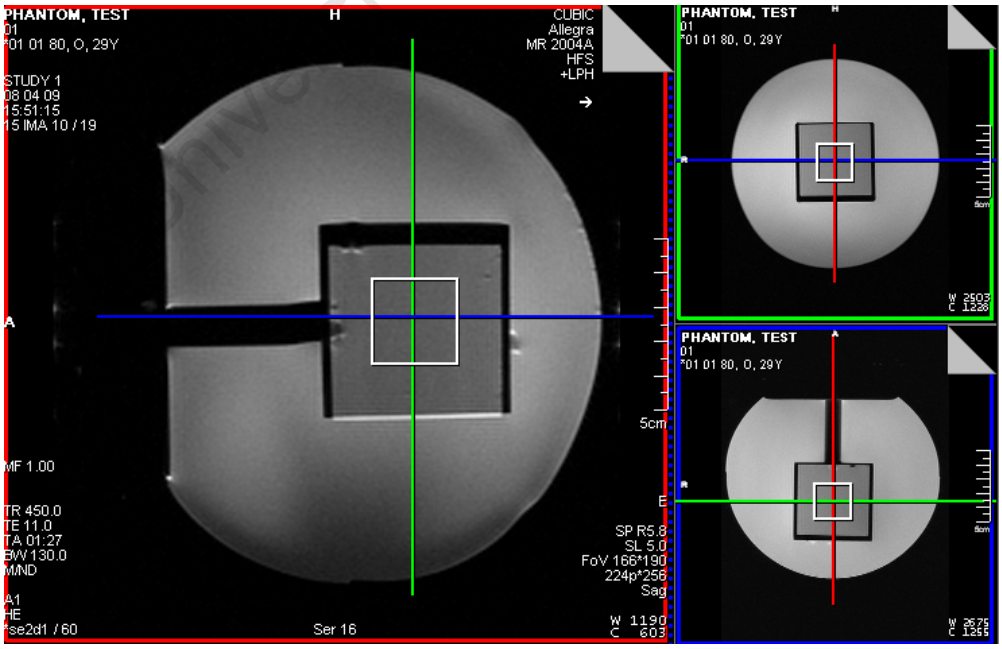

Figure 5.4: Screenshot of the CUBIC's user interface during localisation experiments

The raw spectroscopic data from the scanner (*.rda* files for Siemens scanners) were imported into Matlab, fast Fourier transformed (FFT) into the frequency domain and plotted as shown in figure 5.5.

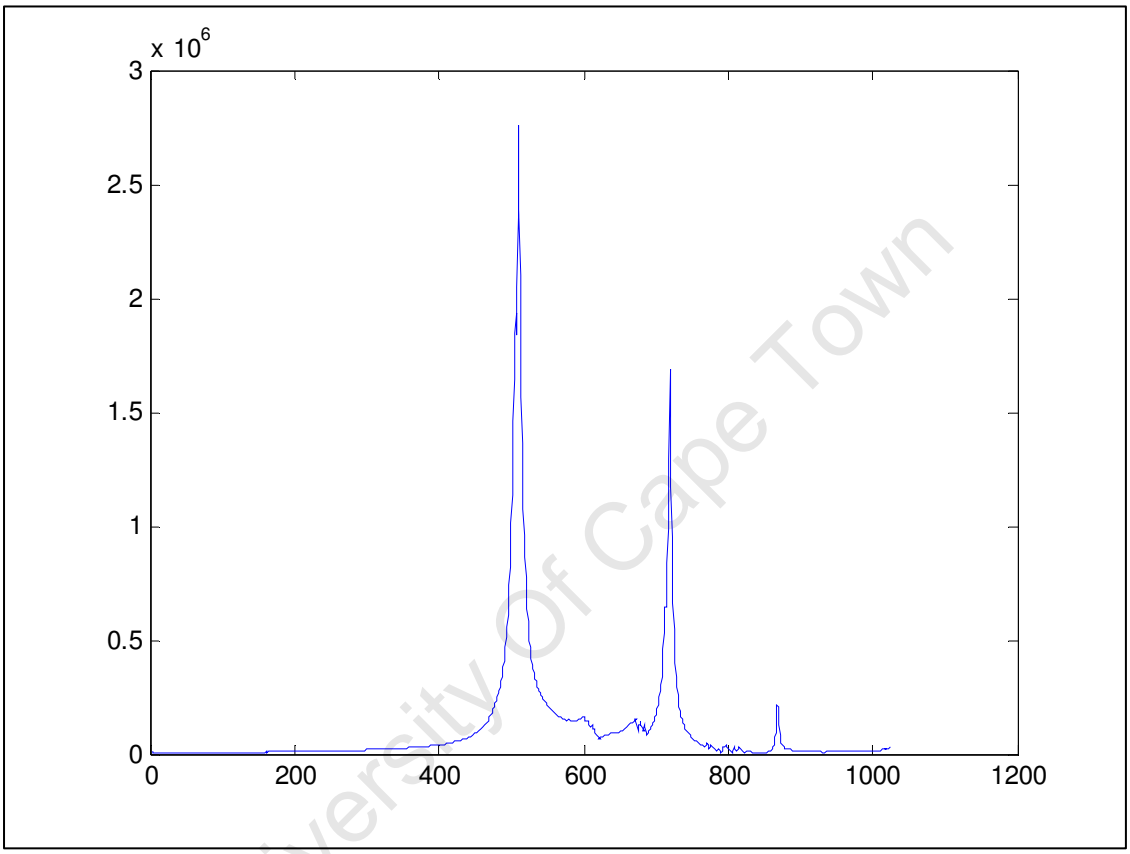

Figure 5.5: Screenshot of Matlab frequency domain data

In order to determine the signal intensities required for the calculation of the selection efficiency (SE), extra volume suppression (EVS), contamination, and water suppression (WS), the area under the metabolite peak was integrated by means of the Matlab *trapz* function.

The FWHM and signal-to-noise ratio (SNR) was determined from LCModel which has a built-in algorithm to determine these parameters.

Certain data sets were acquired with manual shimming as opposed to the automated shimming done by the scanner, in order to compare the spectra obtained by the two methods. The data were Fourier transformed to enable visual spectral analysis of the two types of spectra. It was also analysed in LCModel to determine the line widths and SNR of each individual scan.

5.5.2 Absolute Metabolite Concentrations

The phantom to determine the calibration factor simply consisted of a plastic container containing the NAA solution. Single voxel spectroscopic data with water suppression was obtained at echo times of 30, 135 and 270 ms, since the calibration factor, F, would be sensitive to scanning parameters such as the echo time of the acquisition. Voxel sizes ranged from 18 x 18 x 18 mm^3 to 25 x 25 x 25 mm^3.

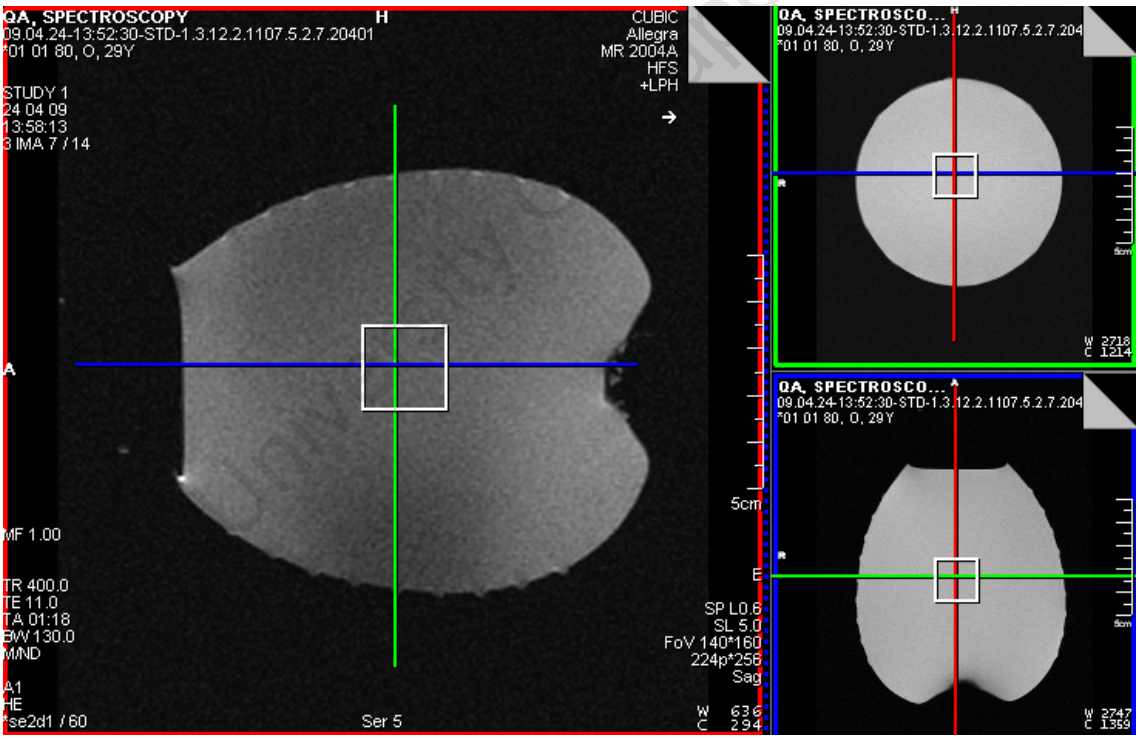

Figure 5.6: Screenshot of scanner during Phantom tests to Determine Absolute Metabolite Concentrations

In order to determine the calibration factor, the raw data from the scanner were processed in LCModel to render the NAA concentration in the phantom in institutional units. Since

the actual NAA concentration in the phantom was known (50 mM), the calibration factor at the respective echo times could be determined.

The water scaling method required that both the water suppressed and –unsuppressed spectroscopic were obtained from the NAA phantom at the same echo and repetition times as for the calibration factor method.
Both these data sets were analysed in LCModel and the additional information regarding the known water concentration in the voxels were input to render the absolute metabolite concentrations.

6. Phantom Results

6.1 Localisation Phantom

6.1.1 General

The initial repetition times for the localisation experiments were set to 8000 ms to eliminate saturation effects which could reduce the signal intensity of the metabolites. This long TR rendered a single scan time of more than nine minutes.

In an effort to reduce scan times, identical voxels were scanned at repetition times of 8000 and 2000 ms respectively, and the signal intensities of the two acquisitions compared. It was found that there is no significant difference between the signal intensities of the two scans (all p-values > 0.1) which show that saturation effects at a repetition time as short as two seconds are negligible. The rest of the scans were then performed with the shorter TR.

6.1.2 Resolution and Signal-to-Noise Ratio

Tables 6.1 to 6.3 list the FWHM and SNR values as a function of voxel size for the different sized cubes acquired with a TR of 2 s as calculated by LCModel.

Table 6.1: Mean FWHM and SNR values for All Localisation Phantom Cube Volumes at TE30

20 mm Cube			30 mm Cube			50 mm Cube		
VOI (mm)[a]	FWHM (ppm)	SNR	VOI (mm) [a]	FWHM (ppm)	SNR	VOI (mm) [a]	FWHM (ppm)	SNR
10	0.035	17.25	10	0.053	13.75	10		
20	0.035	41.5	20	0.015	64.6	20	0.018	70.75
30	0.021	35.75	30	0.035	43	30	0.016	76
40	0.014	64.25	40	0.018	60.8	40	0.022	64.5
50			50	0.016	59.2	50	0.019	49
60			60	0.053	13.75	60	0.017	23
75			75			75	0.022	43.25

[a]length of one side of the cube

Table 6.2: Mean FWHM and SNR values for All Localisation Phantom Cube Volumes at TE135

20 mm Cube			30 mm Cube			50 mm Cube		
VOI (mm)[a]	FWHM (ppm)	SNR	VOI (mm) [a]	FWHM (ppm)	SNR	VOI (mm) [a]	FWHM (ppm)	SNR
10	0.037	15.33	10	0.058	12.5	10		
20	0.041	39.67	20	0.017	49.5	20	0.033	44.5
30	0.024	45.33	30	0.042	28	30	0.018	55.25
40	0.017	85	40			40	0.018	45.75
50			50	0.016	87.25	50	0.019	42
60			60	0.016	89.25	60	0.02	24
75			75			75	0.024	47.25

[a]length of one side of the cube

Table 6.3: Mean FWHM and SNR values for All Localisation Phantom Cube Volumes at TE270

20 mm Cube			30 mm Cube			50 mm Cube		
VOI (mm)[a]	FWHM (ppm)	SNR	VOI (mm)[a]	FWHM (ppm)	SNR	VOI (mm)[a]	FWHM (ppm)	SNR
10	0.038	12	10	0.052	8.25	10		
20	0.041	28.33	20	0.018	49.75	20	0.034	45.25
30	0.024	38.67	30	0.042	28.5	30	0.017	58.5
40	0.02	68.33	40			40	0.019	47
50			50	0.017	71	50	0.02	44.25
60			60	0.015	68.25	60	0.019	21.75
75			75			75	0.027	41.25

[a]length of one side of the cube

6.1.3 Selection Efficiency

In this study, however, the unlocalised NAA signal intensity could not be determined as it was too small compared to the water and choline signals and was lost in the baseline for all 90^{o} FID acquisitions. It was therefore not possible to determine the SE as a percentage, although the localisation profile for the experiments could still be obtained.

Figures 6.1 to 6.3 show these profiles for all three echo times for the 20 mm, 30 mm and 50 mm cubic phantoms, respectively. The vertical line represents the edge of the cube from where the NAA signal intensity should start to form a plateau. A fourth curve has been added to the plots to show the basic line shape during ideal conditions. This curve was calculated based on the principle that the signal intensity is directly proportional to the volume of the selected voxel [4]. This relationship does not appear linear on the plots since the x-axis represents the length of the side of the voxel and not the volume.

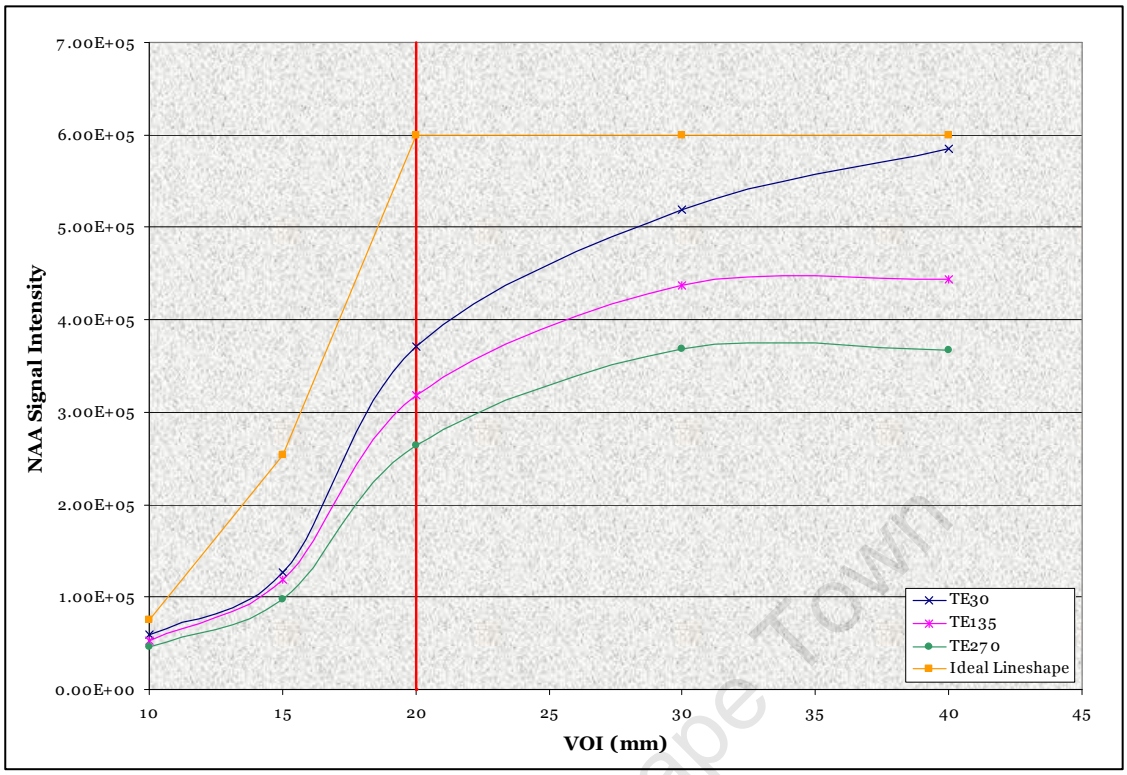

Figure 6.1: Localisation Profile for 20 mm Cube

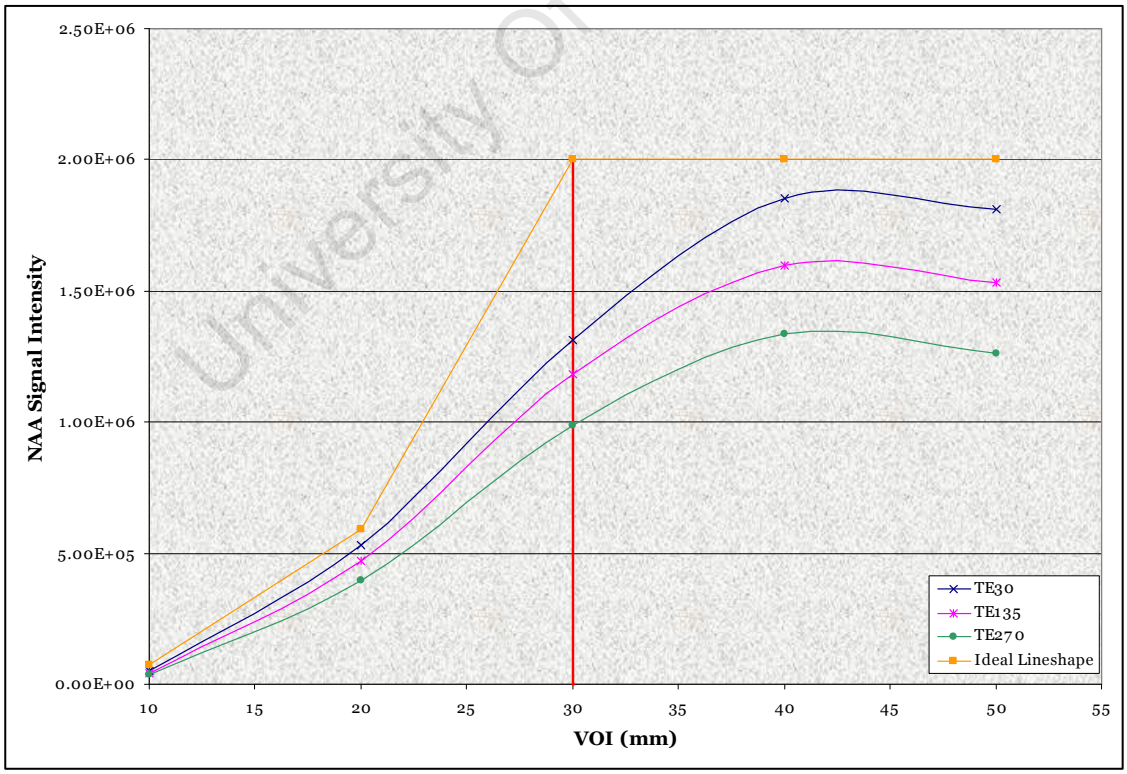

Figure 6.2: Localisation Profile for 30 mm Cube

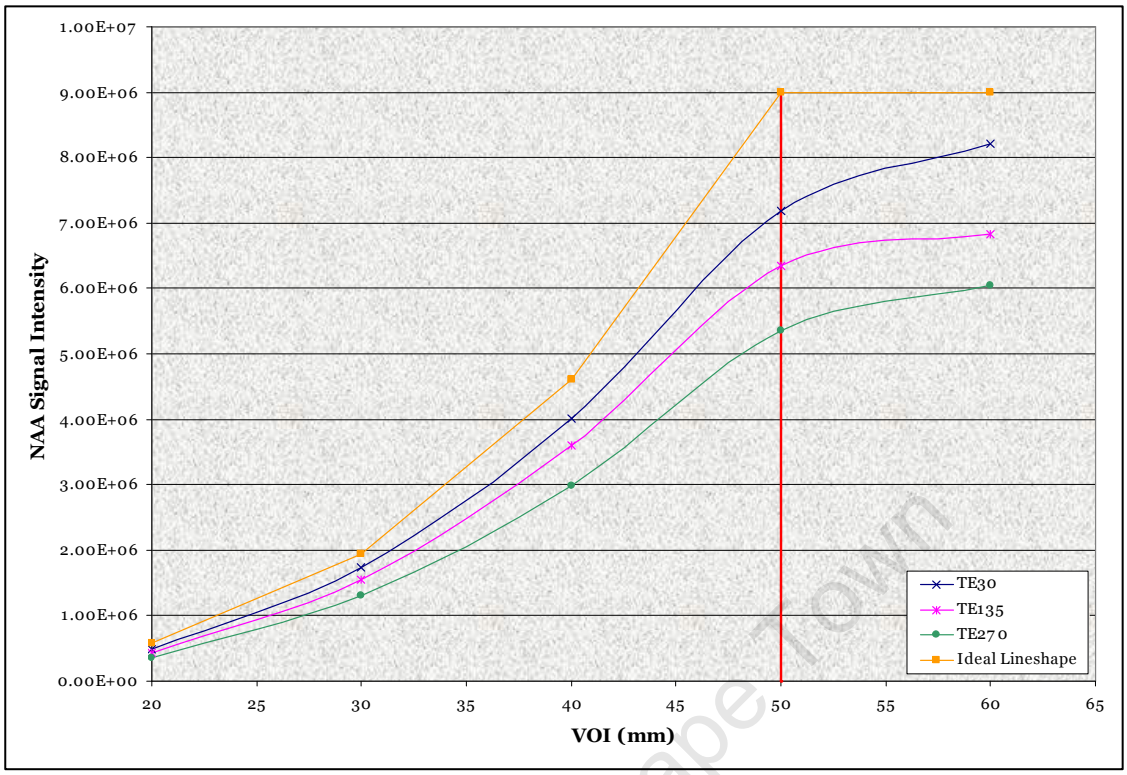

Figure 6.3: Localisation Profile for 50 mm Cube

6.1.4 Extra Volume Suppression

The results for EVS are shown in figures 6.4 to 6.6 for the 3 different sized cubic phantoms, respectively.

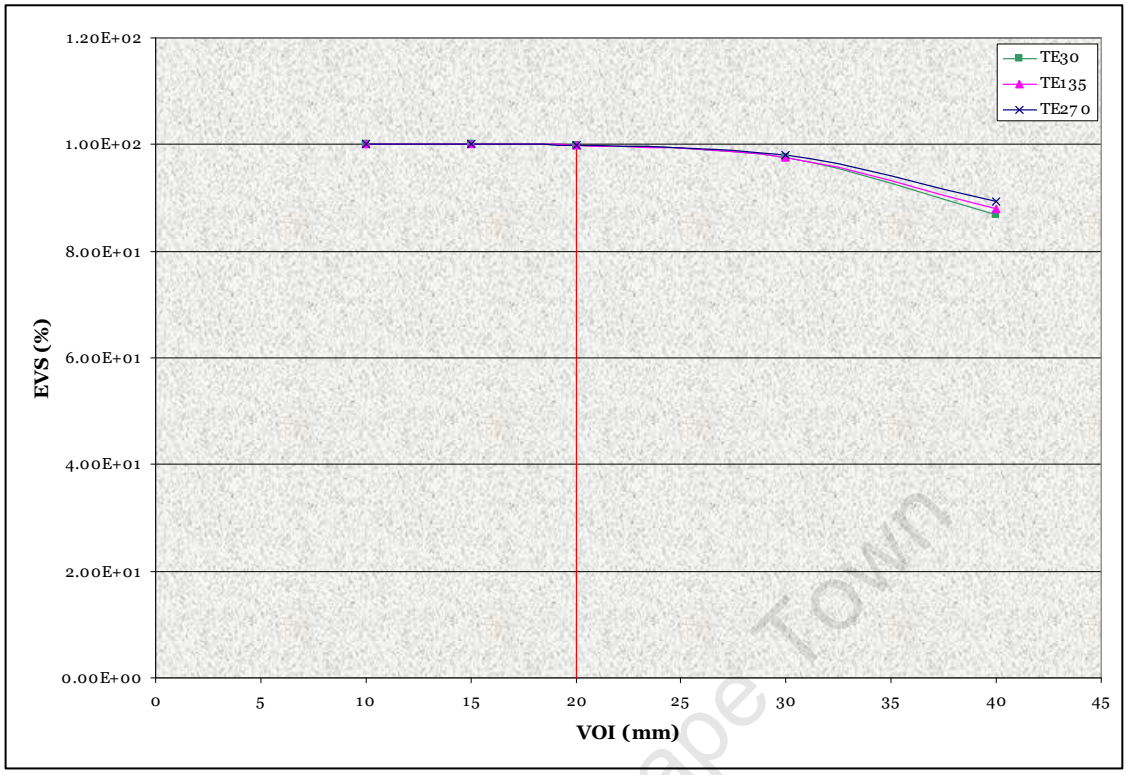

Figure 6.4: EVS for 20 mm Cube

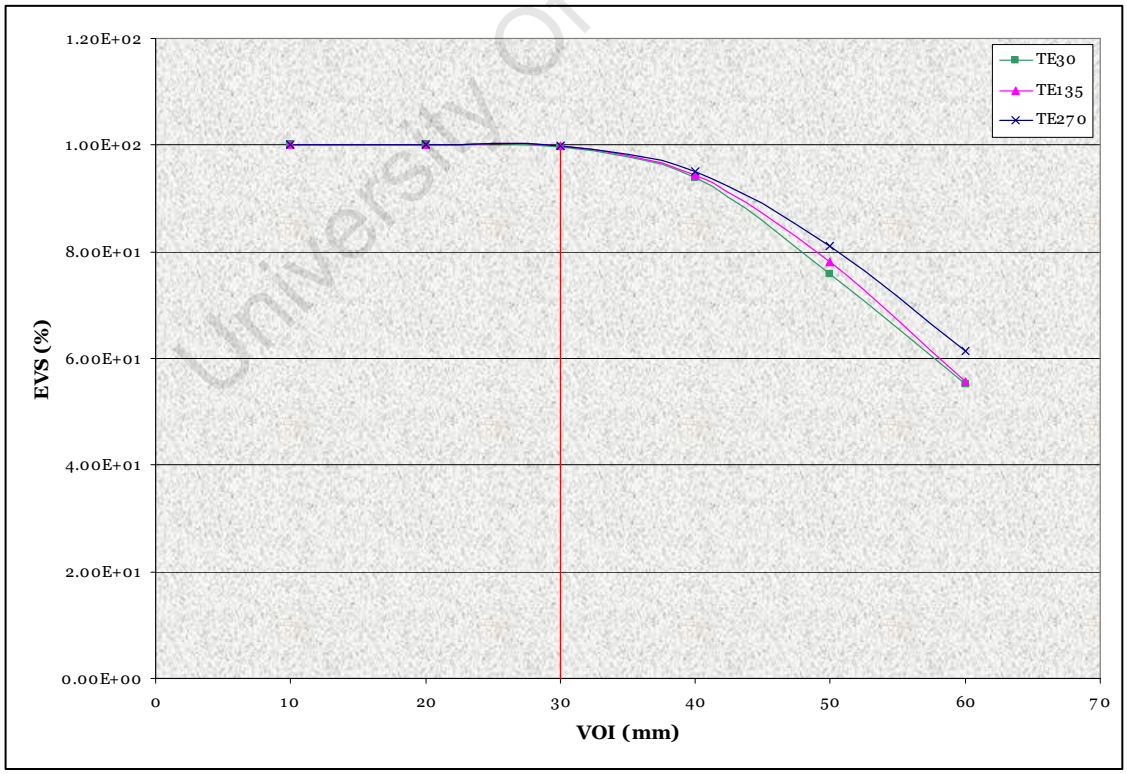

Figure 6.5: EVS for 30 mm Cube

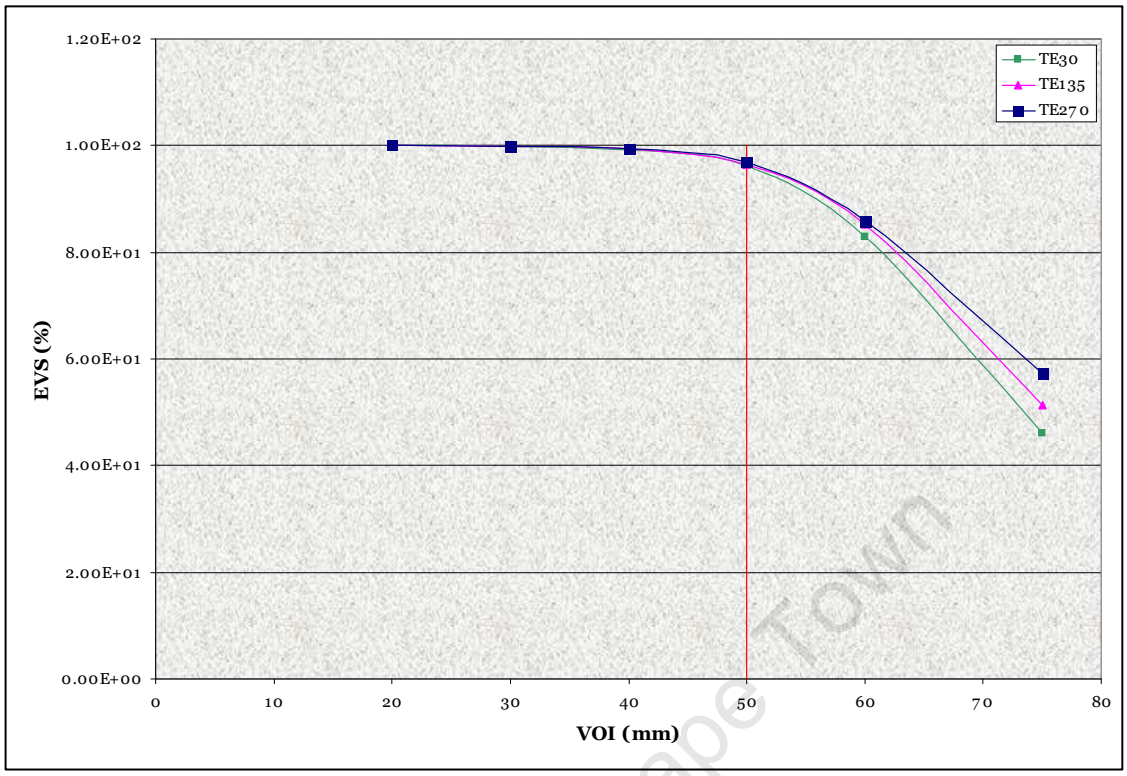

Figure 6.6: EVS for 50 mm Cube

6.1.5 Contamination

Contamination quantitatively assesses the worth of obtained spectra and according to Keevil and Newbold (2001) [14] relays the most information regarding sequence performance. Figures 6.7, 6.8 and 6.9 show the contamination as a function of voxel size for all three echo times for the $(20\ mm)^3$, $(30\ mm)^3$ and $(50\ mm)^3$ cubic phantoms, respectively.

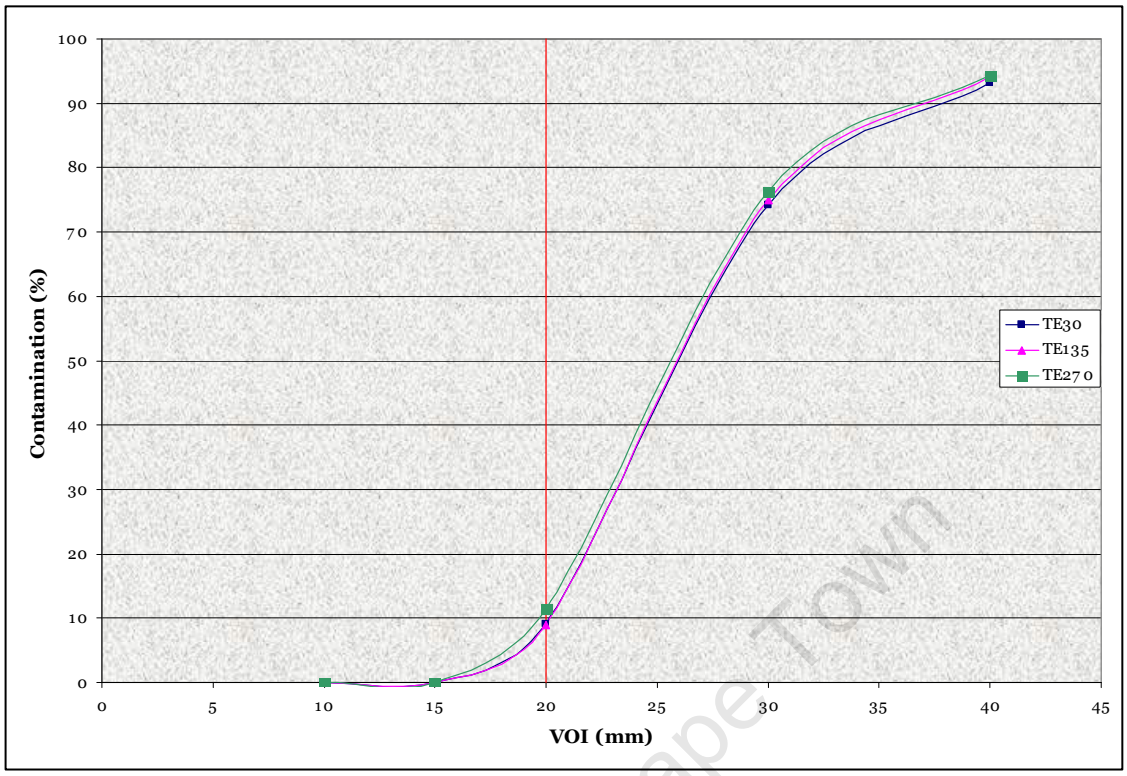

Figure 6.7: Contamination for 20 mm Cube

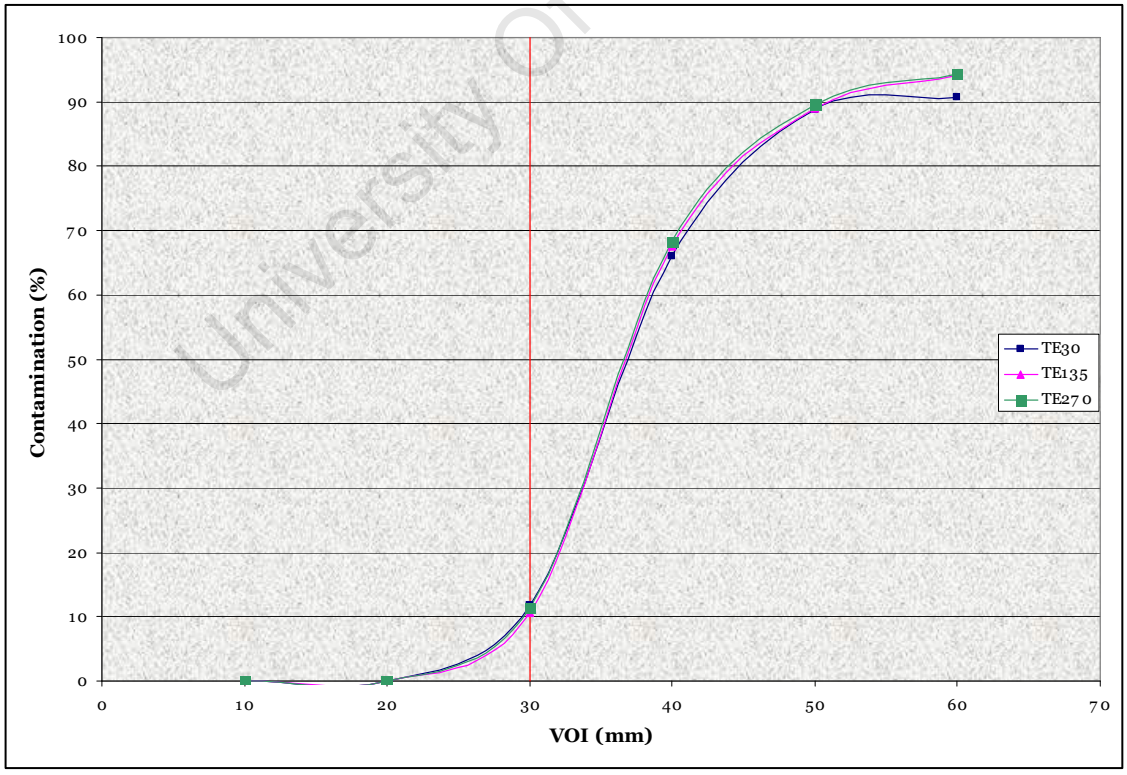

Figure 6.8: Contamination for 30 mm Cube

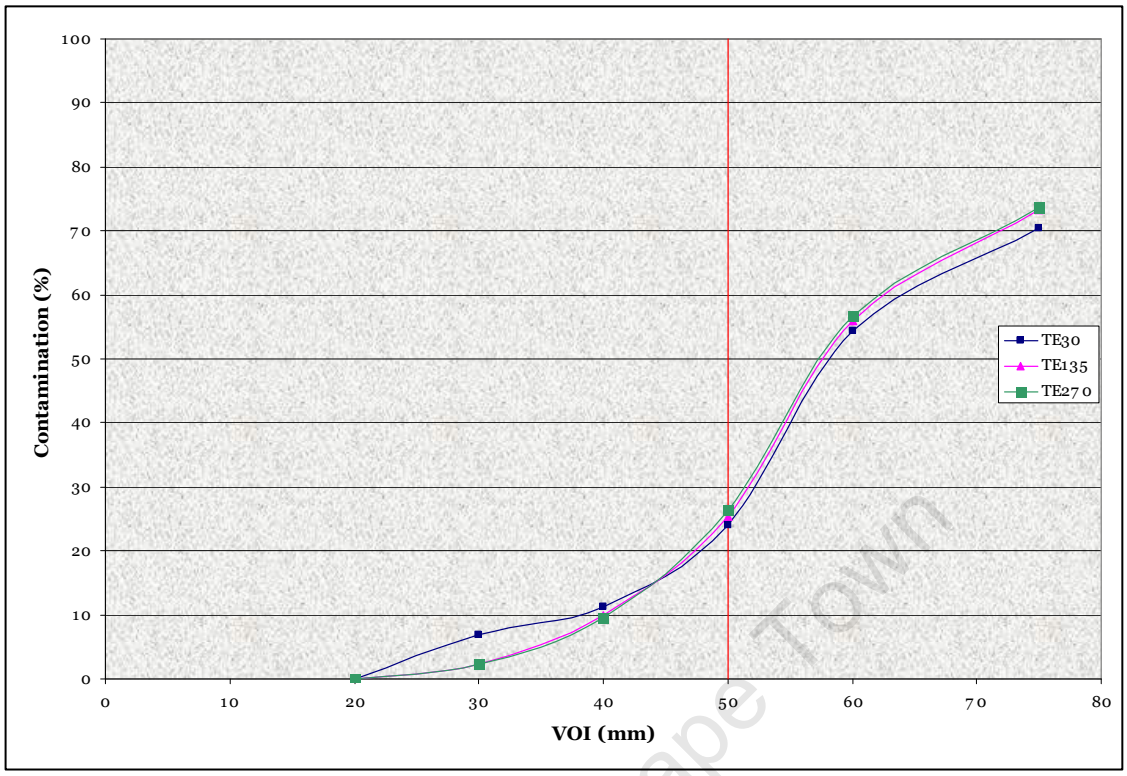

Figure 6.9: Contamination for 50mm Cube

6.1.6 Water Suppression

A random set of raw data were selected for the calculation of the water suppression efficiency for the scanner at CUBIC. The results are shown in figure 6.10.

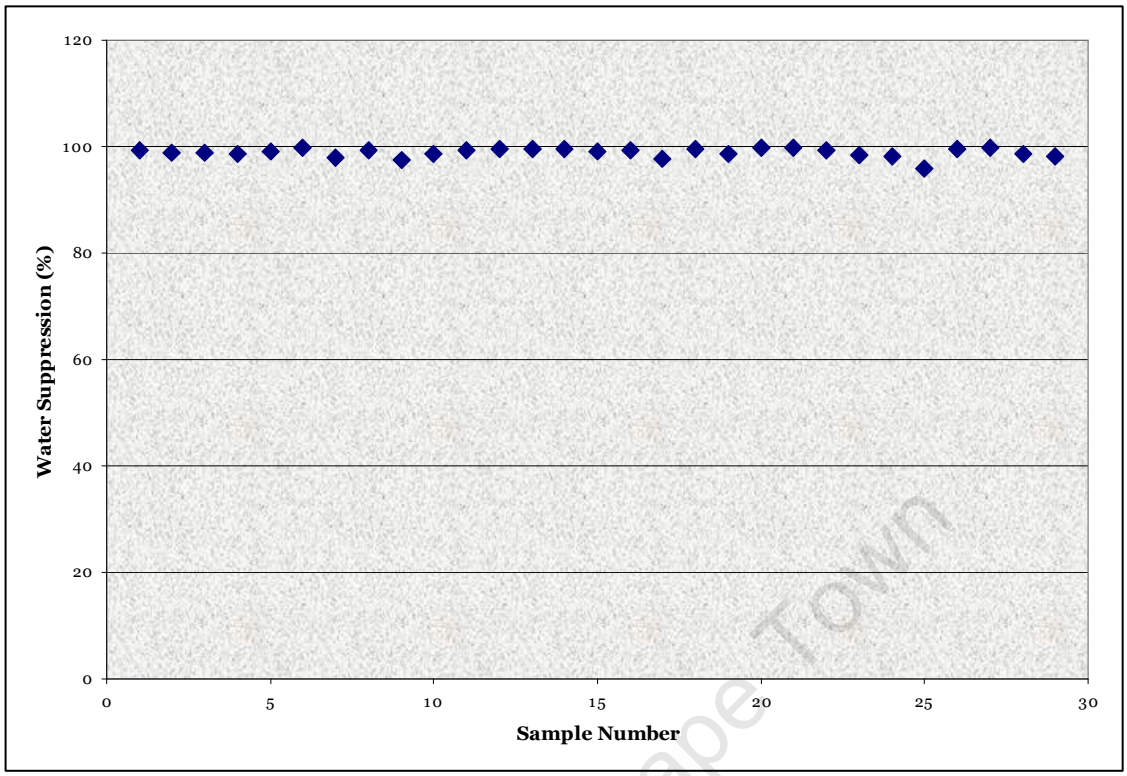

Figure 6.10: Water Suppression Efficiency

6.1.7 Manual vs. Auto-Shimming

The following plots show the spectra obtained with automated and manual shimming in the localisation phantom using the $(20\ mm)^3$ and $(30\ mm)^3$ phantom cubes respectively.

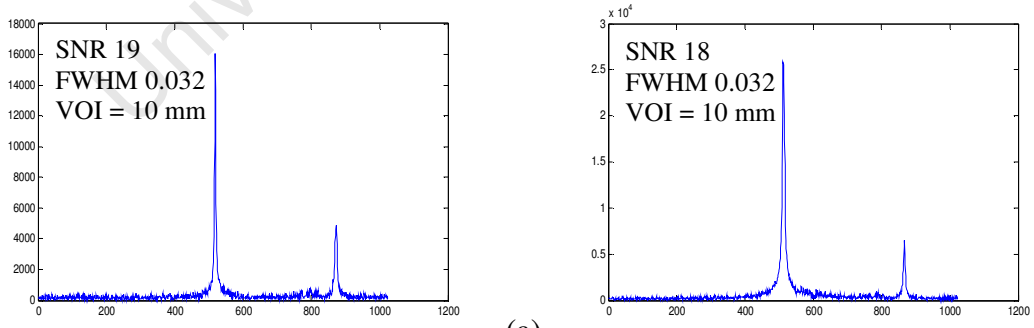

(a)

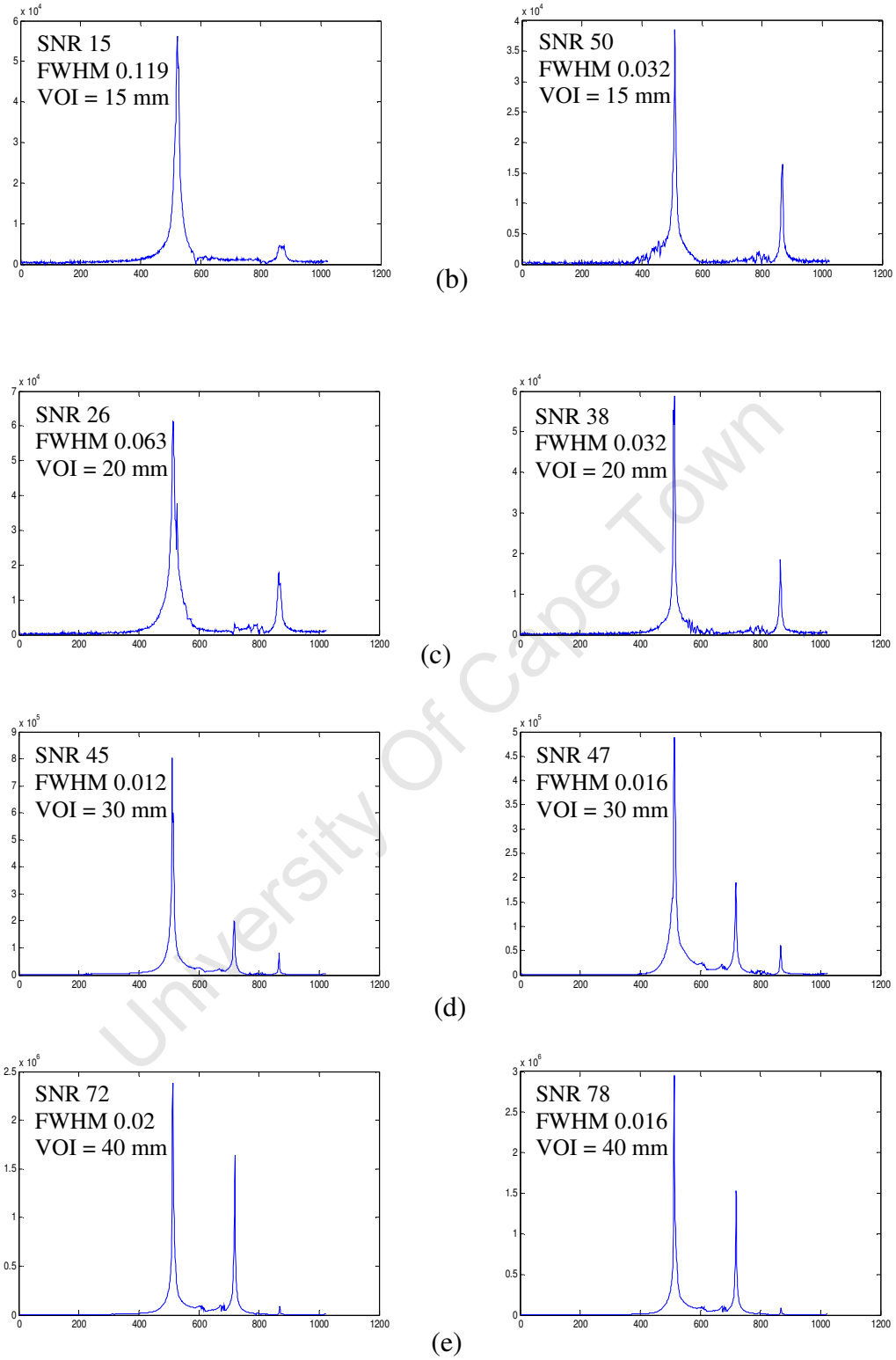

Figure 6.11: Spectra from Localisation Phantom with 20 mm Cube obtained with both automated (left) and manual (right) shimming

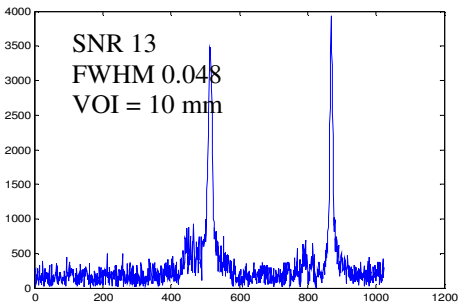

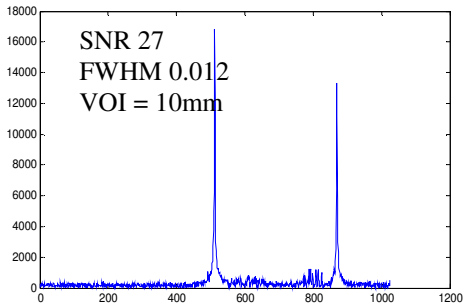

(a)

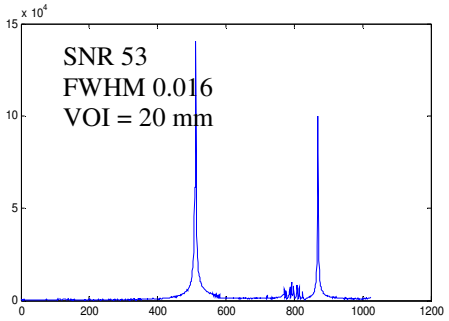

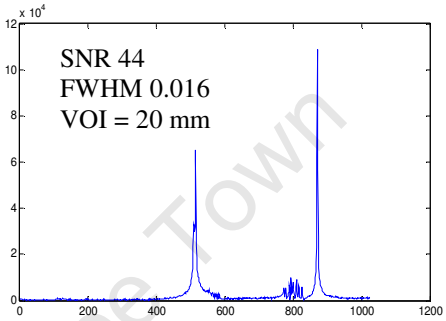

(b)

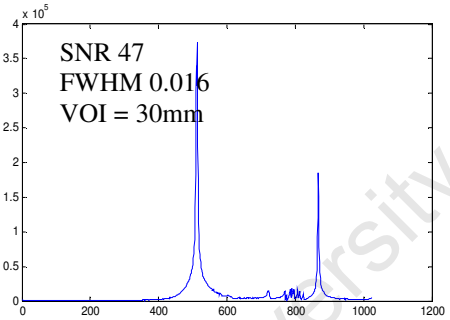

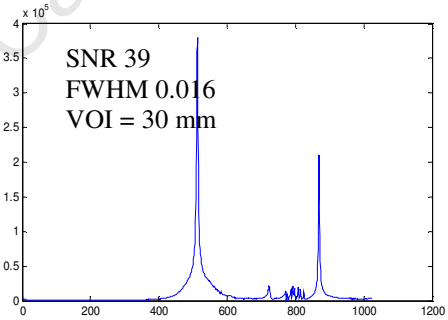

(c)

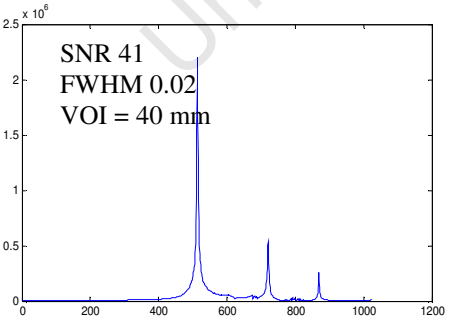

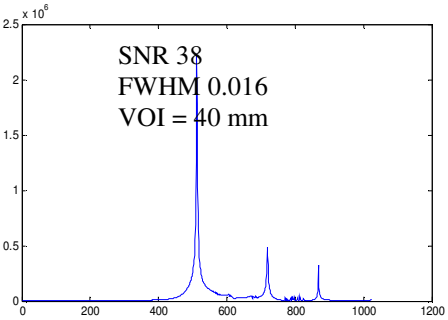

(d)

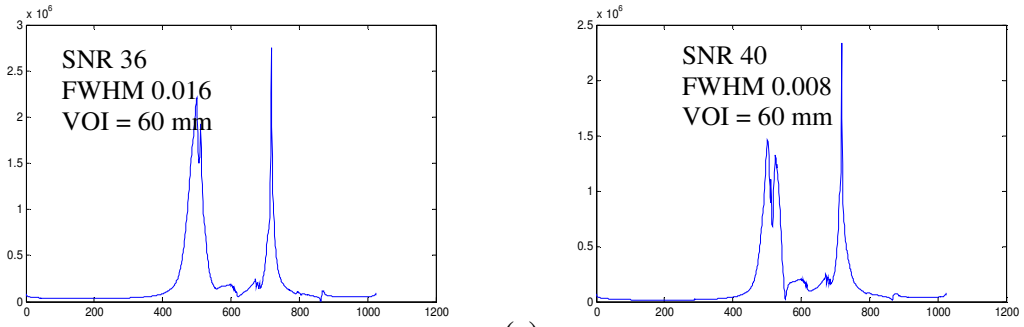

(e)

Figure 6.12: Spectra from Localisation Phantom with 30 mm Cube obtained with both automated (left) and manual (right) shimming

6.2 Absolute Metabolite Concentration Phantom

6.2.1 Calibration Factor

Two phantoms with known concentrations of NAA were scanned on each occasion. The first phantom was used to calculate the calibration factor F using equation 5.5, which was then used to calculate the absolute concentration of NAA in the second (test) phantom

This second phantom contained the exact same solution as the first phantom i.e. a 50 mM NAA solution. The absolute metabolite concentrations for the second (test) phantom were calculated by means of the calibration factor determined from the data obtained from the first phantom. The results are shown in figure 6.13:

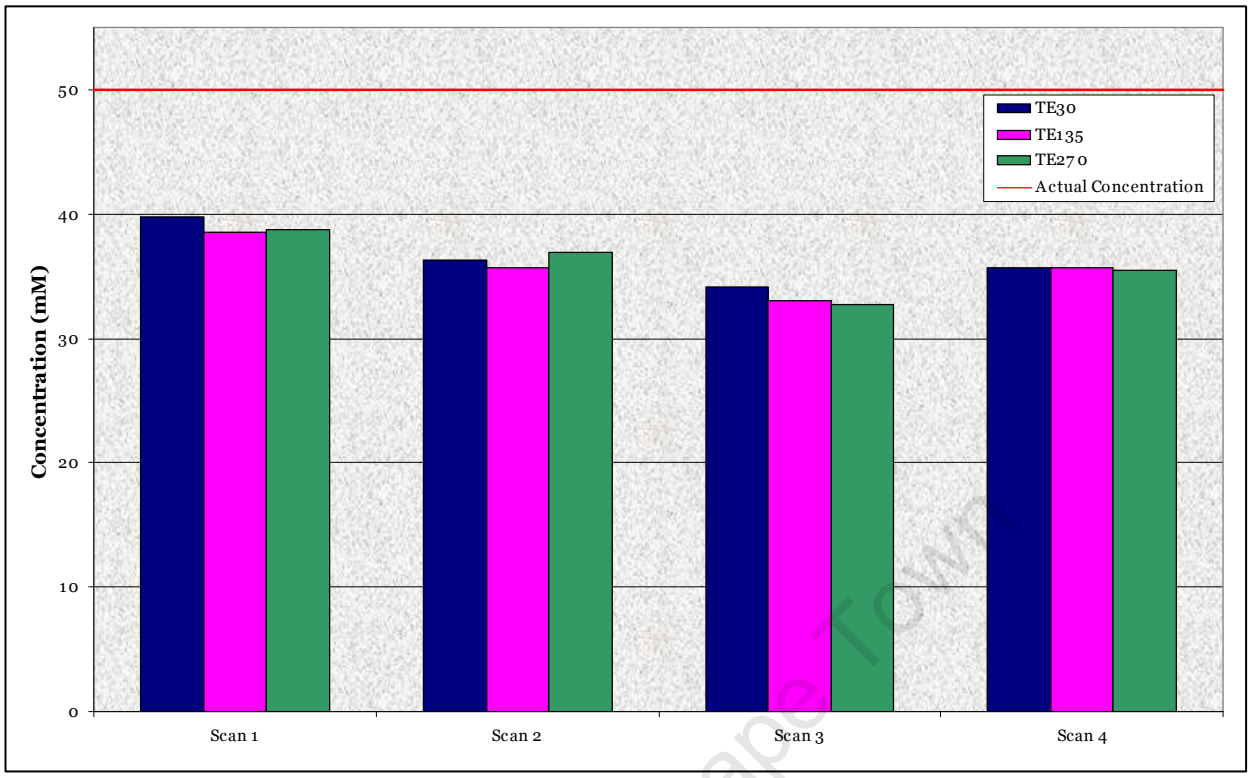

Figure 6.13: Absolute Metabolite Concentration in Phantom as Calculated by the Calibration Factor. The Horizontal line indicates the true concentration in the phantom.

6.2.2 Water Scaling

The unsuppressed water files were also acquired for the second (test) phantom in order to perform water scaling and accurately compare the two quantitation methods. Figure 6.14 shows the absolute metabolite concentration obtained for three different echo times.

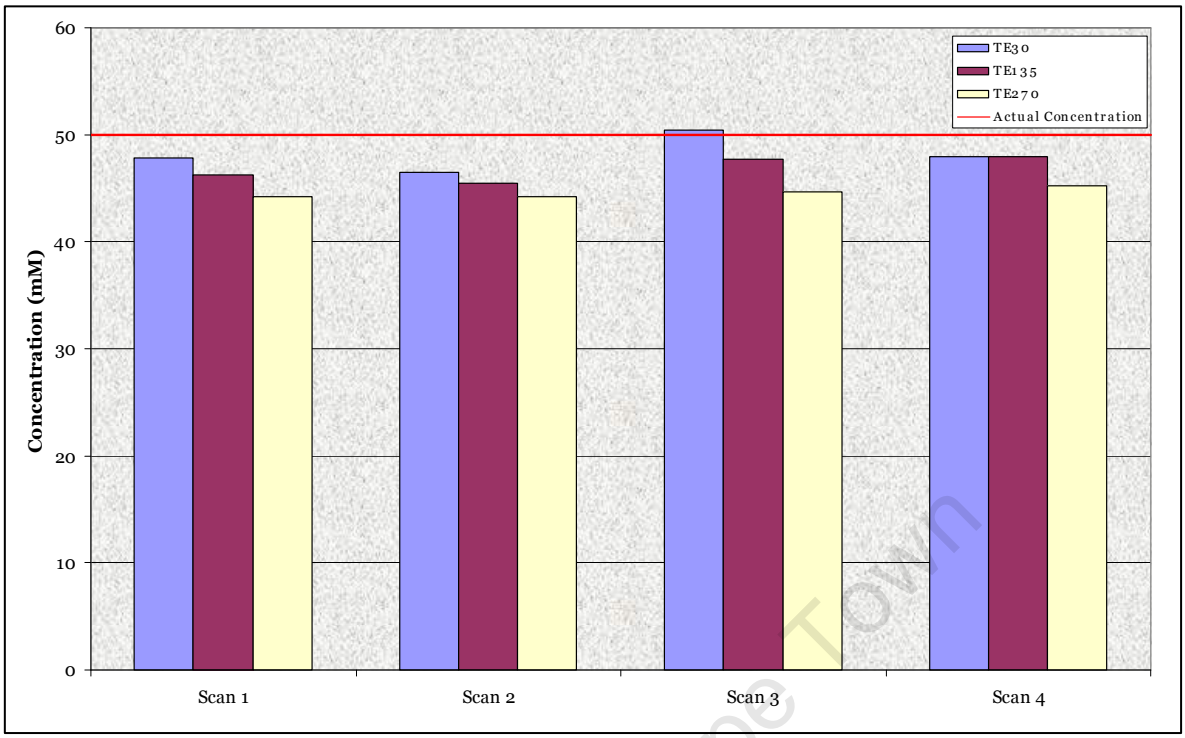

Figure 6.14: Absolute Metabolite Concentration in Second Phantom as Calculated by Water Scaling. The Horizontal line indicates the true concentration in the phantom.

7. Discussion of Phantom Results

7.1 Localisation Phantom

7.1.1 Resolution and Signal-to-Noise Ratio

It is apparent from all three phantom cube sizes that optimal performance regarding the resolution and SNR is achieved at voxel sizes with sides of about 20 mm. This voxel size most consistently yields high SNR and low FWHM, indicating little noise contamination and negligible eddy current effects. Eddy currents are induced by the fast, continuous switching of magnetic gradients in the scanner and can cause artefacts that render spectra useless. Increased FWHM values are a good indicator of the presence of these localised currents.

The fact that the signal intensity increases with increasing voxel size [4] is also clear from the SNR results as these universally increase with an increasing VOI. Below the optimal voxel size of 20 mm, the signal intensity of the metabolite is very small and is subject to much noise i.e. low SNR's (20 and 30 mm cubes).

When voxel sizes exceed the recommended 20 mm, SNR values increase as the signal intensity increases, although the danger of eddy current effects generally start coming into play. However, the FWHM values in table 6.1 are very small until the voxel sizes exceed 60 mm. *In vivo* spectroscopy generally requires data from small voxels (e.g. 20 mm or smaller) as the human body is a heterogeneous structure and large voxels would increase partial volume effects. The results therefore show that eddy current effects are negligible at practical voxel sizes.

7.1.2 Selection Efficiency

We observe the expected decrease in signal intensity with increasing echo times, with the localisation profile for spectra at TE 30 ms being closest to the ideal line shape.

The signal loss from the PRESS profile (section 3.4) of the scanner becomes very apparent when the voxel size coincides with the exact cube size. On each of the selection profiles, the signal intensity deviates most from the ideal line shape when these sizes are the same.

Figure 7.1 graphically illustrates the principle of this signal loss.

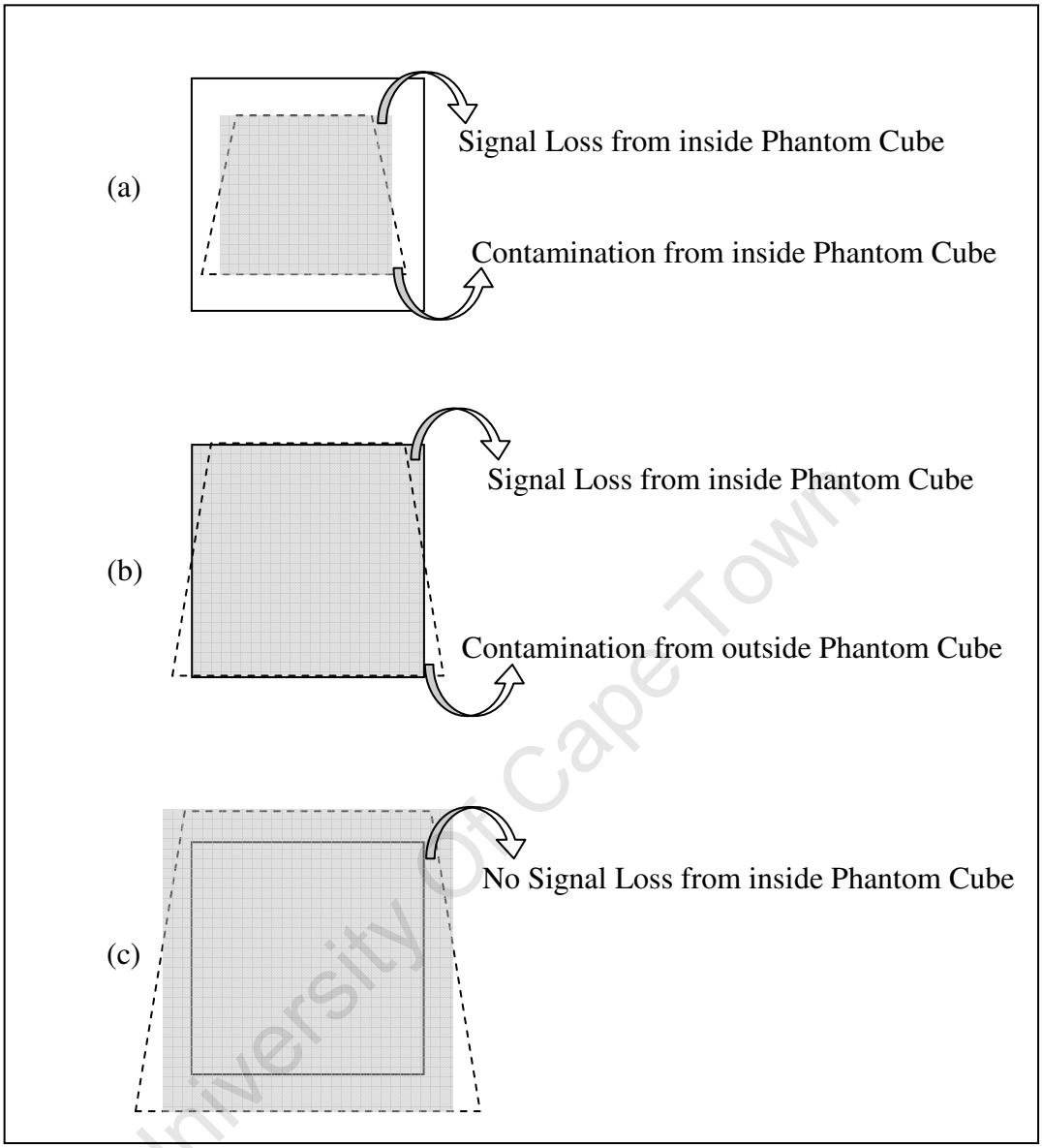

Figure 7.1: PRESS Profile for 30 mm Cube when (a) VOI = 20 mm, (b) VOI = 30 mm and (c) VOI = 40 mm. The shaded area is the VOI as selected by the user, dotted line is the volume actually selected by the scanner. The solid line represents the actual borders of the phantom's cube.

When a VOI with sides of 20 mm is selected in the 30 mm cube (figure 7.1a), the signal loss due to the PRESS profile is cancelled out by the 'contamination' caused by the same effect as the whole localised area is still within the cube. This explains the excellent correlation between the actual signal intensities and the ideal line shapes in the selection profiles where the VOI's are smaller than the cube sizes (figures 6.1 to 6.3). The

exception is the data collected at a VOI of 15 mm in the 20 mm cube, but this can be accounted for by very low SNR's.

The signal loss when the VOI equals the cube size is graphically illustrated by figure 7.1b and in this case the loss is not nullified by the VOI contamination as another metabolite is encountered at the border of the cube. Only when the signal intensity is measured at the next voxel size, is the whole cube covered and therefore the complete metabolite signal obtained. This is clear from the localisation profiles where the signal intensities recover at VOI sizes larger than the cube size and once again follow the ideal line shape quite closely. Similar observations regarding selection profiles have been made in other studies [11, 14]

7.1.3 Extra Volume Suppression

The EVS is close to 100% in the 20 and 30 mm cubes where VOI's are smaller than the cube sizes. In the 50 mm cube, however, the EVS starts decreasing with increasing voxel size from a voxel size of only 30 mm. At the critical point where the voxel size is equal to the size of the cube, the EVS in the 50 mm cube is only 96.2%. This is to be expected, since the contamination from the PRESS profile is a function of the voxel size.

Generally, the contamination from the PRESS profile starts to show when the VOI and cube sizes coincide as is expected from the explanation and figure 7.1 in the previous section. It can therefore be concluded that the current crusher gradient settings are sufficient to eliminate background contamination.

7.1.4 Contamination

The most important point in the figures is where the VOI coincides with the cube sizes. It is at this size that the real effect of the scanner's PRESS profile can be seen. The contamination increases from 12% in the 20 mm cube to 24% in the 50 mm cube – showing that the VOI profile error increases with the selected voxel size, as expected.

The contamination values obtained for the scanner at the CUBIC are well within the ranges of studies performed on other scanners. One such study [14] calculated a contamination value of 35.7% with a 50 mm cube on a 1.5 T Philips scanner. The COMAC-BME study [6] also assessed a range of scanners and found their contamination values to range from 10 to 35% with a 50 mm cube.

Figures 6.7 to 6.9 also show that contamination is independent of echo time – a finding corroborated by the other localisation evaluation studies [6, 14].

7.1.5 Water Suppression

Most scanners have water suppression efficiencies around 98% and the CUBIC's scanner is no different. The water suppression efficiency ranged from 97 to 99.3% as shown in figure 6.10 (mean value 98.84%, standard deviation 0.89). These values are well within accepted limits for MR spectroscopy.

7.1.6 Manual vs. Auto-Shimming

There has been some debate as to the value of time consuming manual shimming in *in vivo* spectroscopy as opposed to the scanner's auto shimming. To this end, I assessed the spectra that are obtained by both means under ideal circumstances in a phantom.

Figures 6.11 and 6.12 allow visual inspection of the spectra obtained by both shimming methods, as well as quantitative analysis through the display of the SNR and FWHM of the relevant spectra. Based on both these evaluation methods and statistical t-testing it is clear that there is no significant difference between the spectra obtained with auto- or manual shimming at intermediate voxel sizes (VOI > 20 mm) under these ideal conditions (all p-values > 0.1).

The spectra from the smallest voxels in figures 6.11 and 6.12 show that manual shimming indeed improved the visual appearance of the spectra as well as the quantitative parameters that accompany them. This finding provides a method to improve spectra when small VOI's are required. Furthermore, in heterogeneous tissues found *in vivo*,

manual shimming should provide higher quality spectra in spite of a slightly longer scan time.

7.2 Absolute Metabolite Concentration Phantom

7.2.1 Calibration Factor

Figure 6.13 shows almost 20% underestimation in the absolute concentration of the second phantom. Considering that this is based on an *in vitro* study, it is fair to assume that more pronounced errors will be encountered when applied *in vivo* due to the heterogeneous nature of the human body. The considerable errors encountered with this method would therefore not make this a feasible technique for determining absolute metabolite concentrations.

7.2.2 Water Scaling

The results of the four different scans show a maximum error of 7% at an echo time of 30 ms which increases up to 12% at a TE of 270 ms. The results are much closer to the actual concentrations than the values obtained using the calibration factor.

The assumption that the calibration factor is a constant is probably a gross oversimplification. In fact, the LCModel manual doesn't recommend this method either [10]. De Graaf [7] proposes a much more complex set of equations to replace the constant calibration factor:

$$[m] = \left(\frac{S_m}{S_r} \right) [r] C_n C_{av} C_{gain} \quad , \qquad \text{(Eq. 7.1)}$$

in which

$[m]$ is the actual concentration of the specific metabolite

S_m is the adjusted metabolite signal intensity

S_r is the adjusted reference metabolite signal intensity

$[r]$ is the actual concentration of the reference metabolite

C_n accounts for the number of equivalent protons

C_{av} is a factor accounting for the number of averages

C_{gain} is an adjustment according to the receiver gain settings

Additional equations are used to calculate the adjusted metabolite signal intensities and these equations account for intrinsic factors such as:

- Nuclear Overhauser effects
- Diffusion
- Scalar coupling
- T_1 and T_2 relaxation
- Localisation profile errors and
- RF pulse imperfections

The intricate details to these equations highlight the simple nature of using a constant to determine AMC's. Equation 7.1 also demonstrates why the water scaling method is more successful than the calibration factor method.

In determining AMC's there must be a reference substance with a known concentration that can be manipulated in order to determine other AMC's. This sounds very similar to the calibration factor method, but is quite different for one simple reason – the reference substance must be scanned at the same time and under the same conditions as the metabolite under investigation.

Conditions within a scanner change from scan to scan and it is therefore essential that the reference substance, whether it is an external or internal reference, is scanned at the same time and within the same conditions – as is done for the water scaling method.

The results from this section clearly show superior performance by the water scaling method and therefore water scaling will be applied in the *in vivo* study described in chapter 8.

8. MRS study of the cerebellar deep nuclei in children with Fetal Alcohol Spectrum Disorder.

8.1 Introduction

Fetal alcohol spectrum disorder (FASD) is the most widely encountered preventable form of mental retardation worldwide and is caused by maternal drinking during pregnancy. In the United States the incidence of FASD is one to three per 1000 live births, while that in the Cape Coloured (mixed ancestry) population in the Western Cape Province of South Africa has been estimated to be 18 to 141 times greater than that [15] - the highest reported incidence in the world. The Western Cape is known for its vineyards and wine production and a very large portion of the Cape Coloured community works on these wine farms. Farm laborers used to be paid, in part, with wine – a remuneration method called the *dop* system. Socioeconomic deprivation combined with the easy access to alcohol, lead to excessive maternal drinking and therefore a high prevalence of FASD in these communities [16]. Even though the *dop* system has been declared illegal, heavy alcohol consumption persists in both the urban and rural Cape Coloured [17, 18].

8.2 Background

8.2.1 Fetal Alcohol Spectrum Disorder

Although alcohol consumption during pregnancy has been known to harm the unborn fetus for centuries, it was only in 1968 that these effects were published in the medical literature [19] in France. In 1973 the term 'fetal alcohol syndrome' or FAS was coined in a paper published by Jones and Smith (1973) [20], but it is only after three further publications by Jones that this condition became widely recognized [19].

Ever since the initiation of these studies there have been challenges associated with the classification of the condition as it became clear that the degree of neurological damage varies with the level and timing of alcohol exposure [19].

Today the term 'fetal alcohol spectrum disorder' (FASD) is used to cover the whole spectrum of conditions that may arise from prenatal exposure to alcohol. The range of

disorders covered by the term FASD were defined in 1996 by the Institute of Medicine (IOM) and elaborated on in 2005 [21]. The different forms of FASD are:

- alcohol-related neurodevelopmental disorders (ARND),
- alcohol-related birth defects (ARBD),
- partial fetal alcohol syndrome (PFAS) without confirmed maternal alcohol exposure,
- partial fetal alcohol syndrome (PFAS) with confirmed maternal alcohol exposure,
- fetal alcohol syndrome (FAS) without confirmed maternal alcohol exposure and
- fetal alcohol syndrome (FAS) with confirmed maternal alcohol exposure.

Each of these classifications has a specified list of criteria that has to be met for a positive diagnosis.

FAS is the most severe form of FASD. These children are characterized by a distinctive craniofacial dysmorphology, including a flat philtrum, thin upper lip, and small palpebral fissures [21]. They also have smaller head circumferences and are subject to growth retardation.

A partial FAS (PFAS) diagnosis requires the presence of two of the three facial features as well as either a small head circumference, signs of retarded growth, or signs of neurological damage. The third group afflicted with alcohol-related neurodevelopmental disorders (ARND) does not have any of the characteristic facial features, but it is known that these children were exposed to alcohol prenatally and there are signs of neurobehavioral deficits. In this group, the lack of the characteristic facial features associated with FAS and PFAS often lead to improper diagnoses and treatment [22]. This group will be referred to as the 'heavily exposed' (HE) group in this study.

8.2.2 Neuroimaging of FASD

Prior to advances in neuroimaging, the neural manifestations of FASD were studied post mortem. These examinations noted prominent anomalies in the neocortex [23], basal ganglia, brainstem, neural tube [24], corpus callosum, hippocampus and cerebellum. Gyral malformations as well as the abnormal placement of neural and glial cells were also seen [25]. A range of other deformities such as hydroencephaly, microencephaly, cerebral disgenesis and malformed ventricles were also noted, but the problem with post-mortem analyses is that the differences in the brain were possibly linked to the cause of death and therefore is not applicable to live brains [24].

The development of neuroimaging technology has simplified the structural and functional study of FASD. Magnetic resonance imaging (MRI) has highlighted more structural anomalies in the FASD brain. Displacement of cerebral structures such as the corpus callosum [26], the vermis of the cerebellum [27] and anterior commisure [25]) has been noted and associated with anomalies in the formation of radial glia that assist neurons with migration during development [23].

Archibald et al (2001) [28] first applied shape and size analysis and found decreased total intracranial volume, with disproportionate reductions in the frontal, parietal and temporal lobes. However, after correction for total brain volume, only the decreased size of the parietal lobes remained statistically significant. Sowell et al (2002a) [29] reported increased gray matter concentrations in the inferior parietal and superior temporal lobes [24]. It has also been shown that poorer performance on the California Verbal Learning Test (CVLT) in participants with FASD is associated with increased cortical thickness in specified regions of the parietal, frontal and temporal lobes [30].

Another study [28] found that the corpus callosum (CC) is subject to inferior, anterior displacement in subjects with FASD, with disproportionate size reduction of the splenium (posterior aspect of CC). The extent of displacement was found to correlate with verbal learning impairment as measured by the CVLT. Bookstein et al (2001) [31] also

determined that the thickness of the CC among alcohol-affected patients could be linked to either poorer executive function (thicker CC) or motor deficits (thinner CC).

The integrity of cerebral white matter in FASD subjects has also been studied by means of diffusion tensor imaging (DTI) in which the fractional anisotropy (FA) is measured. FA measures the degree of directionality in water diffusion. These studies showed decreased FA in cerebral white matter, suggesting poor axonal integrity, less consistent fibre bundles or reduced myelination [32, 33, 34, 35]. Decreased FA in cerebral white matter in rats has previously been linked to reduced axon size, less densely packed fibre bundles, and thinner myelin sheaths [28, 36].

A comprehensive study of the structural, metabolic and functional abnormalities encountered in FASD children (age 8 to 16 years) were performed in 2009 [37, 38]. The rigorous 4-digit FASD classification code was used to classify the subjects into a FAS/PFAS group, a SE/AE (static encephalopathy / alcohol exposed) group, a ND/AE (neurobehavioral disorder / alcohol exposed) group and a healthy control group. The results obtained through rigorous MRI scans confirmed and elaborated on many of the findings mentioned before. Brain volume decreased incrementally between the groups as symptom severity increased. The total brain volume of the FAS/PFAS group was 11% smaller than that for the control group. The same was applicable for the frontal lobe (11 – 18% smaller in total volume, 6 – 9% smaller in relative volume), gray and white matter in the frontal lobe (19% smaller than the SE/AE group), caudate (12 – 14% smaller than the controls), putamen (13% smaller) and hippocampus (9 – 16% smaller). The correlation between the volumes of the all the abovementioned structures, except for the putamen, were negatively correlated with the severity of the FASD diagnosis.

There was no correlation between the midsaggital area of the corpus callosum and the severity of the four groups. A 9% reduction in the area was, however, significant when all the FASD groups were combined and compared to the control group. A decreasing correlation was also found between the length of the corpus callosum and the four groups

ranging from the controls to the FAS/PFAS group (9% shorter in the FAS/PFAS than the controls).

The final structure to be studied was the midsagittal vermis and lobules I to V of the cerebellum. The areas of both these sections were significantly reduced in the FAS/PFAS group compared to the controls, although the correlation between the four groups was not significant.

Magnetic Resonance Spectroscopy (MRS) allows *in vivo* assessment of the local chemistry of tissues. To date, only a handful of studies have used spectroscopic imaging to assess brain damage and changes due to prenatal alcohol exposure. A study using primates [39] reported an increasing ratio of choline to creatine with increasing alcohol exposure in a VOI that includes the thalamus, basal ganglia and adjacent white matter. The authors concluded that this increase is due to the breakdown of cholinergic neurons to serve as an alternative choline source in the production of the neurotransmitter, acetylcholine. Insufficient acetylcholine concentrations were inferred from the cognitive and behavioral impairment of the subjects.

Another study [40] found increased NAA levels in the caudate nuclei in children with FASD, both when measured relative to creatine and as an absolute concentration. NAA is typically used as a marker of neuronal integrity with decreased levels being associated with neurodegenerative disorders such as Alzheimer's. The authors in this study suggest that increased NAA levels can also be an indicator of impaired cognitive function and functional anomalies. Increased NAA concentrations have previously been reported in the prefrontal cortex of pediatric patients with obsessive-compulsive disorder [40].

Astley et al. (2009) [37] used spectroscopy to assess the chemical composition of the fronto-parietal white matter and the hippocampal/basal nuclear region. They calculated absolute metabolite concentrations by water scaling using LCModel. Partial volume correction was not determined by means of bi-exponential curve fitting, as is done in the current study, but by segmentation of the MR image. Three metabolite concentrations

were assessed – NAA, choline and creatine. This study found decreased levels of choline in both the white matter and the hippocampal/basal nuclear region in children with FASD compared to healthy controls, which the authors interpret as being indicative of white matter deficiencies. A very important aspect of the choline signal obtained in MRS, is that only the choline in precursors and breakdown products for cell membranes are NMR visible. The choline located in intact membranes is therefore not included in the choline concentration obtained. Reduced choline reserves could therefore indicate reduced cell membrane integrity as there is less available choline to protect the membrane from stimulus induced depletion of phosphatides. Neither of the other metabolites showed any statistically significant difference.

The author could only find one published spectroscopic study of FASD where the VOI was located in the cerebellum. Fagerlund et al (2006) [41] performed magnetic resonance spectroscopic imaging, a multi-voxel spectroscopic technique, in both a large portion of the cerebrum and the cerebellum. Their results showed decreased NAA to choline and creatine ratios in voxels from the cerebral cortex, white matter, thalamus and cerebellum. Although the authors use the absolute signals with caution, as no correction was done for partial voluming or RF inhomogeneity, the AMC's showed that this finding was due to increased choline and creatine signals. Their interpretation mirrors the finding of the primate study in which cholinergic neurons are broken down to act as a precursor to the neurotransmitter acetylcholine. It should be noted that the voxels utilised in the cerebellum were not specific to certain structures, but included segments from different sections of the cerebellum.

Many studies have been devoted to determine the effect that prenatal alcohol exposure has on the fetal cerebellum. The reason for this is that many of the symptoms displayed by the FASD subjects – behavioural deficits, spatial recognition, motor learning and fine motor control [23] – are characteristically controlled by the cerebellum. The spectroscopic imaging reported here was performed as part of a larger study to examine the neural pathways of short-delay eyeblink conditioning at 9 years of age in children with FASD.

Eye Blink Conditioning

The standard short delay eye blink conditioning (EBC) incorporates a conditioned stimulus (CS), a tone lasting for 750 ms combined with an unconditioned stimulus (US), a puff of air to the eye during the last 100 ms of the tone which elicits a reflexive eye blink. Repeatedly pairing the CS with the US, leads the eye blink becoming a conditioned response where subjects blink at exactly the right time to avoid the puff of air to the eye. Figure 8.1 shows a typical EBC setup. It has been shown that EBC is well established by age five months, with healthy control children achieving the same level of conditioning as adults [42].

Figure 8.1: Experimental Setup for EBC

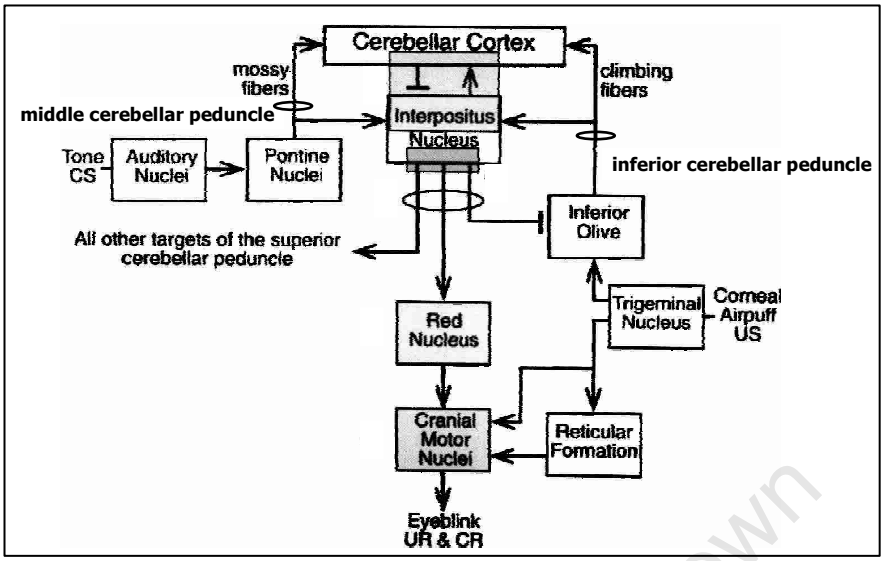

Figure 8.2: Neural Pathways of EBC [43]

The neural pathways of EBC have been extensively studied in animal models and been shown to be cerebellar dependent. As illustrated in figure 8.2, the tone (CS) is received by Purkinje cells in the cerebellar cortex from the auditory and pontine nuclei via the middle cerebellar peduncle. The signal from the air puff (US) is received by the trigeminal nucleus, transmitted to the inferior olive and delivered to the cerebellar cortex via the inferior cerebellar peduncle. Both the received signals are then sent from the Purkinje cells to the cerebellar deep nuclei and transmitted via the superior cerebellar peduncle to the red nucleus, and on to the appropriate motor neurons that produce the eye blink response [43, 44]. Neural plasticity is essential for successful EBC as new neural pathways need to be created in order to create the conditioned response.

The effect of prenatal alcohol exposure on EBC has been reported in several studies. Green et al. (2002 a,b) [45, 46] noted disrupted EBC in rat weanlings and adults that were exposed to alcohol during the third trimester. Cell loss as well as altered neuronal activity was found in the cerebellar deep nuclei of the rats. Loss of Purkinje and granule cells was linked to prenatal binge drinking in similar studies [47, 48]. Apoptosis also lead to degeneration of cells in various cerebellar regions, even after only a single binge exposure [49].

In the 5-year old follow-up of a Cape Town longitudinal cohort (Jacobson et al., 2008), a remarkably striking EBC deficit was noted in children with prenatal alcohol exposure [61]. None of the children with full FAS met criteria for conditioning at the end of three sessions. Only 33.3% of the PFAS children and 37.9% of the heavily exposed children met criteria for conditioning at the same time, compared to 75% of the control children (Table 8.1). It was also striking that 75% of the microcephalic children, who have IQ's similar to those of the children with FAS, did meet criteria for conditioning after three sessions. Figure 8.3 shows a significant increase in the percent conditioned responses from session one to two in the control and microcephalic children, compared to very little improvement in the alcohol exposed children. It has been suggested that EBC may be a potential biomarker for FAS.

Table 8.1: Comparison of the number of children that met criteria for conditioning as a function of diagnosis [18]

	Alcohol-exposed			Nonexposed		
	FAS	Partial FAS	Heavy exposed	Control	Micro-cephalic	Total
Session 1	0 (0.0)	2 (11.1)	3 (10.3)	4 (20.0)	1 (25.0)	10 (12.3)
Session 2	0 (0.0)	3 (16.7)	2 (6.9)	9 (45.0)	2 (50.0)	16 (19.8)
Session 3	0 (0.0)	1 (5.6)	6 (20.7)	2 (10.0)	0 (0.0)	9 (11.1)
Total conditioned	0 (0.0)	6 (33.3)	11 (37.9)	15 (75.0)	3 (75.0)	35 (43.2)
Total *N*	10	18	29	20	4	81

Values are number of children (%) who met the criterion of at least 40% conditioned responses (CR) in a session. Each child is shown in the session in which s/he first met the CR criterion.

As part of a study aimed at investigating the various components of the EBC circuit, MRS was performed in the cerebellar deep nuclei in order to assess the integrity of the tissue in this region. The results may indicate whether abnormalities in this region could be the source of the eye blink conditioning deficit observed in children with FASD.

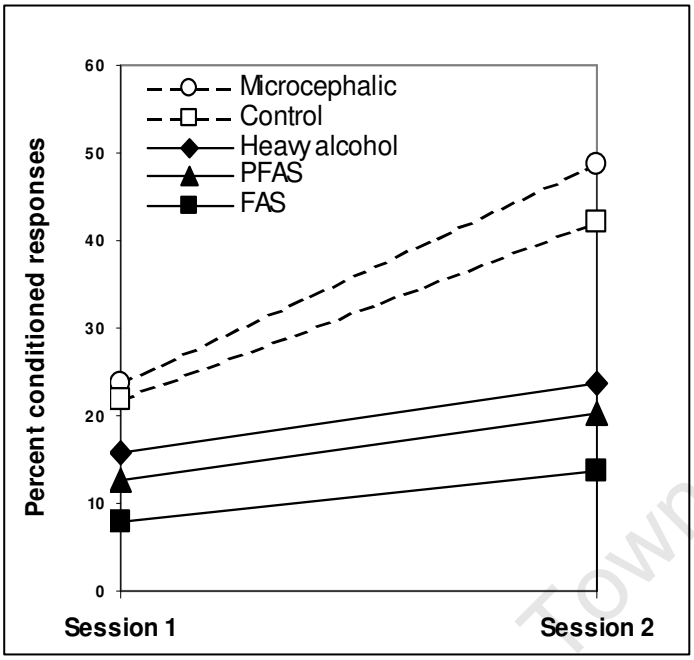

Figure 8.3: Percent Conditioned Responses from Session One to Session Two [18]

The Effects of Prenatal Alcohol Exposure on the Developing Nervous System

Extensive studies of the effect that prenatal alcohol exposure has on the developing nervous system have been performed [23, 50] and some results have shown that alcohol exposure during certain gestational periods tend to produce specific abnormalities in the developing fetus. Alcohol exposure in the first trimester tends to lead to the characteristic facial deformations and neural tube abnormalities. Exposure in the second trimester affects neuronal migration via radial glia, which has been linked with behavioural deficits. The anomalies associated with exposure in trimester three are deficient myelination, neuronal loss, breakdown of glial cells and severe cerebellar and hippocampal damage. The research has therefore shown that certain cells are more vulnerable to the effects of alcohol than others.

There are several mechanisms that are thought to damage the CNS via prenatal alcohol exposure [50]. A very popular hypothesis is that ethanol primarily attacks the glial cells during development, rather than the neurons themselves [25]. This theory is supported by many actual abnormalities found in the FASD brain. The first supporting fact is the displacement of various structures in the alcohol exposed brain. During development,

neurons migrate from the germinal zone to their intended position by means of radial glia. This means that any anomalies associated with the radial glia would explain the structural differences in the FASD brain. A separate study has confirmed that ethanol has a detrimental effect on astrogliogenesis which directly affects the radial glia as they are precursor cells to the glial cells astrocytes [51]. More concrete evidence has been found in which Green et al (2002a) [45] showed that general prenatal alcohol exposure leads to loss of Purkinje and deep nuclear cells in the cerebellum.

Astrocytes are vital to the maintenance and homeostasis of neuronal cells. It regulates potassium ions in the extracellular fluid, which is crucial for the production of proper nerve impulses, and also takes up the released neurotransmitters, glutamate (Glu) and GABA, and transforms them into glutamine (Gln). Anomalies associated with these glial cells therefore affect proper signal transduction [25].

The deficient fractional anisotropy from the DTI study mentioned in the previous section supports the glial-cell-theory. Oligodendrocytes are primarily responsible for the myelination of axons in the CNS. The reduced integrity of white matter largely points to deficient myelination

8.3 Methods

Participants

Participants for this study were recruited from two different cohorts, namely the Cape Town longitudinal cohort of Sandra and Joseph Jacobson who received MRI scanning as part of their 9-year follow up, and another group of children who were recruited to pilot the neuroimaging procedures planned for the above study. Subject recruitment for each of these cohorts is described below. Participants were 38 right-handed 9-13 year old children with FAS/PFAS, 31 age and gender matched controls, and 10 heavily exposed children.

Recruitment of Cape Town Longitudinal Cohort

During the period from 1999 to 2002 pregnant women were recruited from an antenatal clinic in Cape Town in an area where there is known to be heavy alcohol consumption [18]. Pregnant woman who admitted to consuming alcohol during pregnancy were invited to participate in the study. A child born to a mother consuming at least fourteen drinks a week or who partakes in binge drinking was considered to be heavily exposed. The next mother who visited the clinic and who drank less than one drink per day or seven drinks per week, and who did not binge drink, was invited to participate as a control subject.

Recruitment of Pilot Cohort

In 2005, older siblings of the above cohort who were 8-12 years of age at the time, were recruited for a functional MRI study of the neural correlates of number processing. Additional children were identified by screening all of the 8- to 12-year-old children from an elementary school in a rural section of Cape Town, where there is a very high incidence of alcohol abuse among local farm workers [52]. A subset of the children in this cohort received MRI scanning a second time to pilot the procedures for the neuroimaging component of the 9-year follow-up of the longitudinal cohort.

FASD diagnosis

The FASD diagnoses were made according to the revised Institute of Medicine criteria [31]. Each child was examined for growth and FAS dysmorphology by two expert dysmorphologists during a clinic conducted in 2005; a subset who could not attend the clinic was examined by one dysmorphologist [18]. There was substantial agreement among the examiners on the assessment of all dysmorphic features, including the three principal fetal alcohol-related features—philtrum and vermilion measured on the Astley and Clarren (2001) [53] rating scales and palpebral fissure length (median $r = .78$).

Data Acquisition and Analysis

All spectroscopic data was acquired on the 3 T Siemens Allegra (Siemens Medical Systems, Erlangen, Germany) MRI scanner at the Cape Universities Brain Imaging Centre (CUBIC) using single voxel spectroscopy.

A PRESS sequence with echo time 30 ms and voxel size 20x12x16 mm^3 was used to acquire spectroscopic data in the cerebellar deep nuclei of all the subjects. The position of the cerebellar deep nuclei was determined by means of a T_2-weighted MRI sequence. Iron deposits in the nuclei reduce the signal in this region, rendering the nuclei as dark regions surrounding the fourth ventricle (figure 8.4). A typical *in vivo* MRS repetition time of 2000 ms was used; 128 data sets were acquired and averaged. The vector size of the free induction decay (FID) was set to 1024 complex data points and a spectral frequency of 123.26 MHz was used. All scans were acquired using automated shimming procedures.

Water suppressed and – unsuppressed data were acquired for each voxel in order that water scaling (section 5.4.2) could be used to calculate absolute metabolite concentrations in LCModel. In order to perform partial volume correction (PVC), the unsuppressed water signal was also acquired at a range of echo times – 30 ms, 50 ms, 75 ms, 100 ms, 144 ms, 500 ms and 1000 ms. These datasets were acquired under circumstances identical to the suppressed water signal, but with only 2 averages.

The signal intensities of the range of unsuppressed water signals were plotted as a function of the echo times. Bi-exponential curve fitting was applied according to equation 5.7 to determine the water signal contributions from brain tissue and CSF. As specified in section 5.4.3, the ratio between white and gray matter should be estimated. Since the deep nuclei consist of gray matter, the T_1 and T_2 values used in equation 5.7 were those of gray matter. These values at 3 T are as follows:

- $T_{1,csf}$ = 4000 ms [54]
- $T_{2,csf}$ = 2470 ms [55]
- $T_{1,bw}$ = 1283 ms [54]
- $T_{2,bw}$ = 93 ms [55]

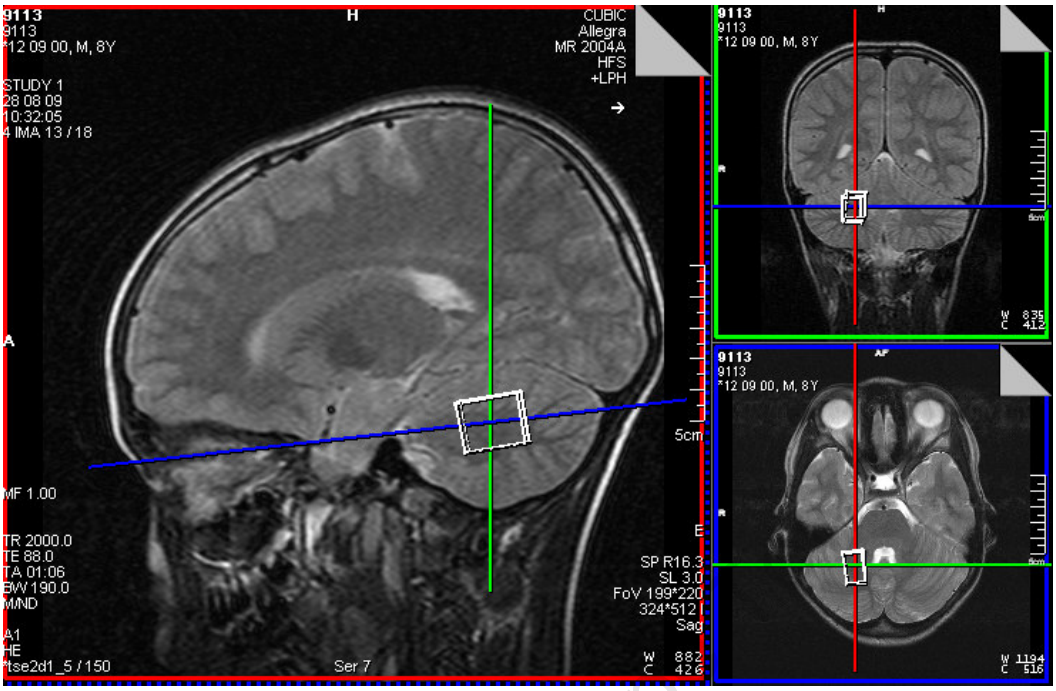

Figure 8.4: User Interface during *in vivo* MRS Data Acquisition in FASD study

The PVC was performed by means of SigmaPlot's [56](version 11) curve fitting function. An example of the bi-exponential curve fitting plot is shown in figure 8.5. In this plot the CSF contribution is 40% and brain tissue 60% of the total signal.

This plot shows clearly that the sum of the contributions from CSF and brain tissue renders the total water signal. Once the CSF and brain tissue fractions are obtained, the water concentration in the VOI can be determined by equation 5.6 and entered into the LCModel execution script.

The final AMC results rendered by LCmodel were categorized and statistical analyses were performed using SigmaPlot (v11) software [56]. In these tests a p-value less than 0.05 was deemed sufficient for statistical significance.

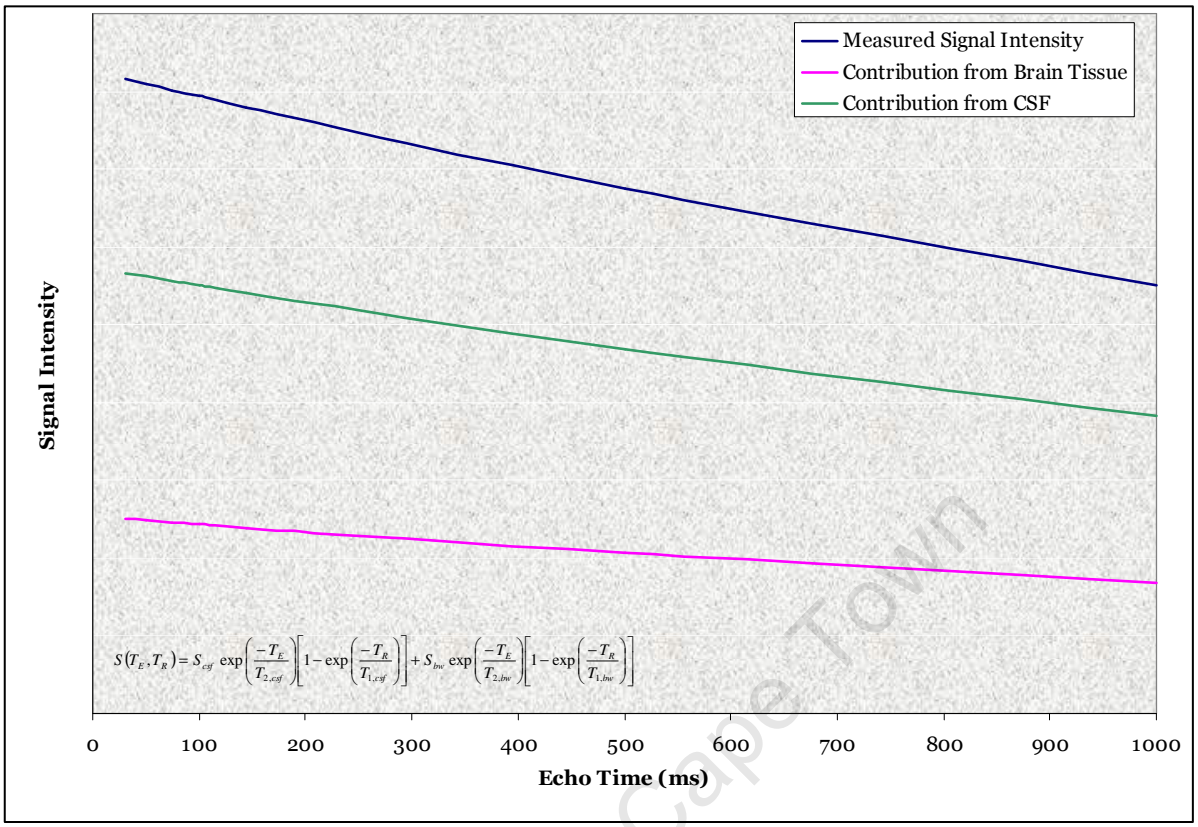

Figure 8.5: Example of Bi-exponential curve fitting where S_{CSF}:S_{BW} is 2:3

Exclusion criteria

Several exclusion criteria were applied to all the spectroscopic data in order to extract only the most reliable results. Quantitative criteria were in the form of the Cramér-Rao lower bounds (CRLB) calculated by LCModel. Datasets with CRLB values greater than 20% were discarded. Each spectrum was also visually assessed with respect to (1) insufficient water suppression, (2) wild baselines, and/or (3) patient motion.

After applying the above exclusion criteria, I report data for 22 (10 male) right-handed 9-13 year old (mean age 10.0 years) children with FAS/PFAS, 23 (12 male) age and gender matched controls (mean age 10.9 years), and 8 (6 male) heavily exposed children (mean age 9.4 years). Of these, 16 of the children with FAS/PFAS, 7 of the controls, and all the heavily exposed subjects were from the longitudinal cohort. The participant characteristics are summarized in table 8.2.

Table 8.2: Subject Characteristics for subjects that provided usable MRS data

	Control	Heavily Exposed	PFAS	FAS
Mean Age (SD)	10.9 (1.4)	9.4 (0.2)	9.9 (1.0)	10.2 (1.6)
Mean IQ (SD)	75.5 (9.7)	74.5 (5.4)	67.2 (8.5)	63.4 (6.3)
Number of Males	12	6	7	3
Number of Females	11	2	8	4
Total Number of Subjects	23	8	15	7

For the MRS data analyses, the FAS and PFAS children were combined into a single group, denoted FAS/PFAS.

8.4 Results

8.4.1 Partial Volume Correction

Partial volume correction yields negligible contribution from CSF to the total signal intensity in the VOI for all the subjects. Dynamic curve fitting according to equation 5.7 produced a mean R^2 value of 0.983 with a standard deviation of 0.007 when the CSF fraction was set to zero.

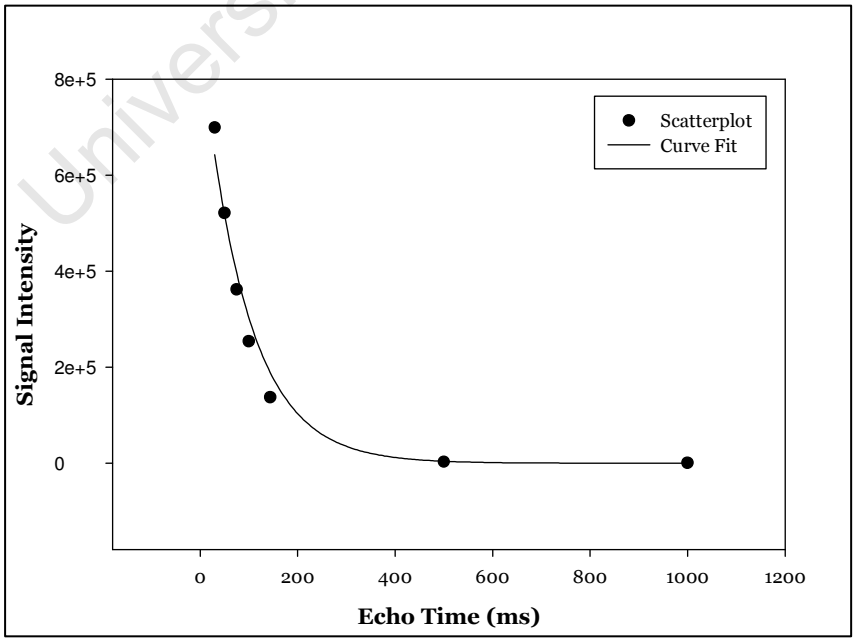

Figure 8.6: Example of Bi-Exponential Curve Fitting

8.4.2 Absolute Metabolite Concentrations in the Deep Cerebellar Nuclei

Table 8.3 lists both the mean absolute metabolite concentration and the mean metabolite ratio to creatine in the cerebellar deep nuclei for each group of subjects for all metabolites measured.

Of all the metabolites studied, only the myo-inositol (mI) and total choline (tCho) concentrations differ significantly between the control and FAS/PFAS groups ($p < 0.05$).

None of the absolute metabolite concentrations were significantly correlated with either age of IQ.

Table 8.3: Mean Results for all Metabolites Studied. Standard deviation in Brackets

	Absolute Metabolite Concentration (mM)			Metabolite Ratios (/Cr)		
	Control	HE	FAS/PFAS	Control	HE	FAS/PFAS
Glu	6.3 (0.9)	5.7 (0.4)	6.2 (1.0)	1.1 (0.2)	1.1 (0.2)	1.1 (0.1)
GPC	1.6 (0.2)	1.4 (0.2)	1.5 (0.3)	0.27 (0.04)	0.26 (0.02)	0.26 (0.02)
Ins*	5.3 (0.8)	5.2 (1.1)	4.6 (0.8)	0.9 (0.1)	1.0 (0.1)	0.8 (0.1)
NAA	6.1 (0.7)	6.2 (0.5)	6.0 (0.9)	1.1 (0.2)	1.2 (0.2)	1.1 (0.2)
GPC+PCh*	1.6 (0.2)	1.4 (0.2)	1.5 (0.3)	0.27 (0.03)	0.26 (0.02)	0.25 (0.03)
NAA+NAAG	7.9 (0.9)	8.2 (0.8)	7.9 (1.0)	1.4 (0.2)	1.5 (0.2)	1.4 (0.1)
Cr+PCr	5.9 (0.8)	5.5 (0.9)	5.7 (0.8)	1.0 (0.0)	1.00 (0.0)	1.00 (0.0)
Glu+Gln	8.3 (2.0)	6.3 (0.8)	7.5 (1.6)	1.4 (0.3)	1.2 (0.3)	1.3 (0.3)

** Control and FAS/PFAS Groups differ significantly ($p < 0.05$)*

Myo-Inositol

The mean myo-inositol concentration is significantly less (Figure 8.7) in the FAS/PFAS subjects compared to the controls (t-test, $p = 0.005$). The concentration for the heavily exposed subjects does not differ significantly when compared to either the FAS/PFAS or the control groups (t-test, $p = 0.18$ and 0.89 respectively).

There is a statistically significant correlation (Pearson correlation, p = 0.006) between absolute mI concentration and alcohol exposure (correlation coefficient = 0.378) (Figure 8.8).

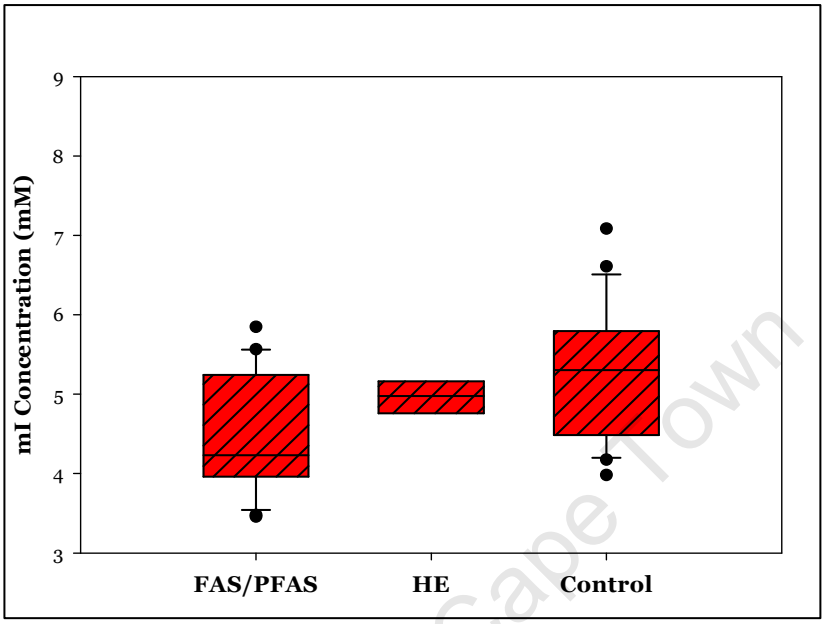

Figure 8.7: Box and whiskers plot of the Mean Absolute Myo-Inositol Concentration in the cerebellar deep nuclei. Error bars represent 95% Confidence Intervals

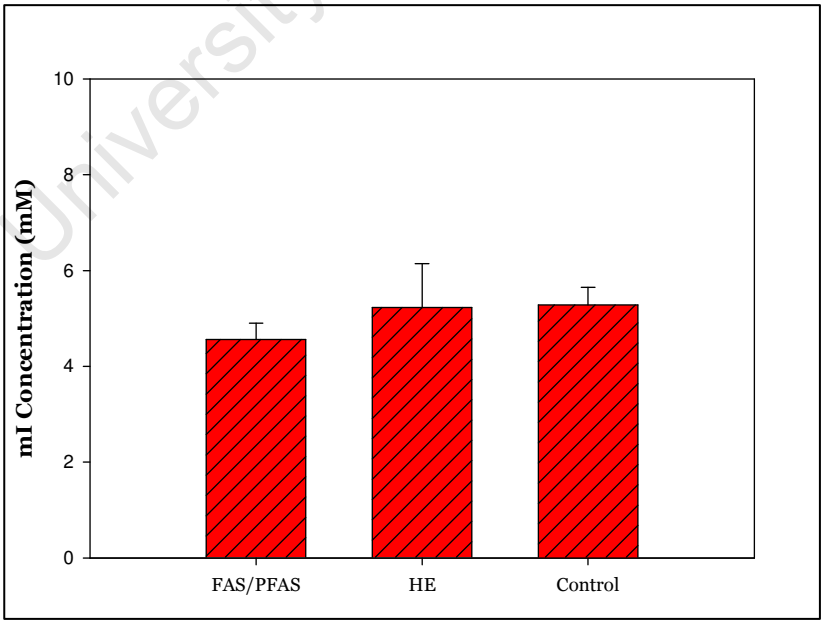

Figure 8.8: Mean Myo-Inositol Concentrations in Deep Cerebellar Nuclei as a function of alcohol exposure. Error bars represent 95% Confidence Intervals

Choline

Reductions in the total choline (tCho) concentrations between the FAS/PFAS and control subjects were found to be significant after statistical analysis (Kruskal-Wallis one way analysis of variance on ranks, $p = 0.006$), while the difference between the heavily exposed and control subjects only tended towards significance (Kruskal-Wallis one way analysis of variance on ranks, $p = 0.078$).

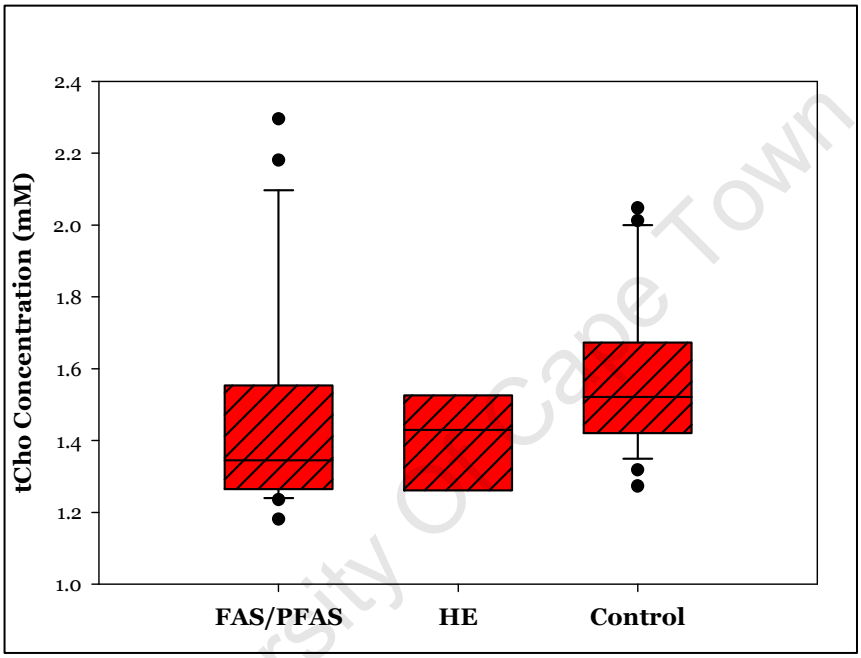

Figure 8.9: Box and whiskers plot of the mean absolute total Choline Concentration in the cerebellar deep nuclei. Error bars represent 95% Confidence Intervals

8.5 Discussion

8.5.1 Partial Volume Correction

While we expected partial volume artifact, due to the close proximity of the cerebellar deep nuclei to the fourth ventricle, there was no significant contribution from this to the signal.

8.5.2 Absolute Metabolite Concentrations in the Deep Cerebellar Nuclei

The full function of most metabolites is still not understood, which makes the interpretation of the results found in any spectroscopic study very difficult. Varying

levels of myo-inositol and choline have been implicated in many medical conditions including Alzheimer's disease, obsessive-compulsive disorder, Down's syndrome and bipolar mood disorder [57]. Reduced myo-inositol and total choline has been reported previously in the study of thyrotoxic Graves's disease, hepatic encephalopathy and hyponatremia [58].

There is great uncertainty as to the function of myo-inositol with regard to spectroscopic studies. Initially, mI was thought to be a marker of glial cells [58], although more recent studies have shown that mI is present in neuronal cells as well. In spite of these results, many studies still link mI results to the glial cell population, specifically to astrocytes [59].

mI is also considered a crucial part of the phosphoinositide (PI) – phospholipase C (PLC) pathways in the CNS [57] as mI is a precursor to the PI second messenger system. Inositol phospholipids are part of cell membranes mainly in the form of phosphatidyl-inositol-(4,5) biphosphate (PIP_2). PLC in turn hydrolyses the PIP_2 into the second messengers inositol 1,4,5-trisphosphate (IP_3) and diacylglycerol (DAG). The IP_3 facilitates the flow of Ca^{2+} out of the neurons, which is one of the main functions of the PI – PLC pathway. A steady supply of mI is therefore needed to maintain proper signalling between neurons. Shimon et al (1998) [60] attributed the psychopathology of a schizophrenia patient where decreased mI was found in the post-mortem brain, to this mechanism.

Choline is a vital component of cell membranes, but, as mentioned before, the choline in intact membranes is not NMR visible [40]. This means that the amount of choline detected by *in vivo* spectroscopy is only made up of cell membrane precursors and breakdown products. Increased Cho levels are therefore common in neurodegenerative diseases such as Alzheimer's [61].

In spite of the fact that Cho in intact membranes are NMR invisible, a decrease in this metabolite has been interpreted as decreased cell density in other studies [62]. Decreased mI levels in children with FAS/PFAS could therefore indicate that the cell decrease is

among glial cells, as mI is regarded by some as a glial cell marker. Astley et al (2009) [37] also noted that choline is more abundant in glial cells than in neurons, which would strengthen the theory of the decreased glial cell population. If this is actually the case, the results obtained in this study also support the glial-cell-theory as proposed by Guerri (2001) [25].

A common denominator between choline and myo-inositol, is that they both are important constituents in cell membranes. The finding of Astley et al (2009a) [37] that decreased choline could indicate decreased cell membrane integrity due to less available choline to remedy the depletion of phosphatides also suggests a decrease in myo-inositol. Reduced cell membrane integrity could therefore account for the results obtained in this study.

In spite of the fact that the deep cerebellar nuclei in the FASD child has not been studied before, the concentrations obtained fall within valid the concentration value range and the trends are reflected in other studies, albeit in other regions of the brain.

9. Conclusions

The typical parameters to assess the performance of MRS consistently presented values that are in agreement with published data [6, 14]. This supports the conclusion that the spectroscopic performance of the scanner at CUBIC is similar to the performance of scanners elsewhere. The fact that eddy current effects are almost negligible, suggests that the 3 T Siemens Allegra is partially superior to other spectroscopic scanners.

There is a significant inverse correlation between myo-inositol concentration in the cerebellar deep nuclei in children with prenatal alcohol exposure and the severity of prenatal alcohol exposure. Reduced total choline was also noted in this area. These results suggest either decreased membrane integrity or decreased glial cell populations in the deep cerebellar nuclei of children with FAS/PFAS. More specific studies regarding the role of myo-inositol and choline in the deep cerebellar nuclei should be performed in order to obtain information that could lead to better interpretation of the results.

References

1. Podo F, Bovée WMMJ, De Certaines J, Leibfritz D, Orr JS. Quality assessment in *in vivo* NMR spectroscopy: I. Introduction, objectives, and activities. *Magnetic Resonance Imaging* 1995; 13(1):117 - 121
2. Marshall I, Wardlaw J, Cannon J, Slattery J, Sellar RJ. Reproducibility of metabolite peak areas in 1H MRS of brain. *Magnetic Resonance Imaging* 1996; 14:281 – 92
3. Deganonkar MN, Pomper MG, Barker PB. Quantitative proton magnetic resonance spectroscopic imaging: regional variations in the corpus callosum and cortical gray matter. *Journal of Magnetic Resonance Imaging* 2005; 22(2):175 – 9
4. Bovée WMMJ, Keevil SF, Leach MO, Podo F. Quality Assessment in *in vivo* NMR spectroscopy: II. A protocol for quality assessment. *Magnetic Resonance Imaging* 1995; 13(1):123 - 129
5. Leach MO, Collins DJ, Keevil S, Rowland I, Smith MA, Henrikson O, Bovée WMMJ, Podo F. Quality assessment in *in vivo* NMR spectroscopy: III. Clinical test objects: Design, construction, and solutions. *Magnetic Resonance Imaging* 1995; 13(1):131 - 137
6. Keevel SF, Barbiroli B, Collins DJ, Danielsen ER, Hennig J, Henriksen O, Leach MO, Longo R, Lowry M, Moore C, Moser E, Segebarth C, Bovée WMMJ, Podo F. Quality assessment in *in vivo* NMR spectroscopy: IV. A multicentre trial of test objects and protocols for performance assessment in clinical NMR spectroscopy. *Magnetic Resonance Imaging* 1995; 13(1):139 - 157
7. De Graaf RA. *In vivo* NMR spectroscopy: Principles and techniques. 2nd ed. Yale University, Connecticut, USA: John Wiley and Sons, Ltd; 2007
8. Pavia DL, Lampman GM, Kriz GS. Introduction to spectroscopy. 3rd ed. Washington: Thomson Learning; 2001
9. Keevil SF. Spatial localisation in nuclear magnetic resonance spectroscopy. *Physics in Medicine and Biology* 2006; 51:R579 – R636
10. Provencher SW. LCModel & LCMgui User's Manual. 2007. Available from: http://S-provencher.com

11. Keevil SF, Porter DA, Smith MA. A method for characterising localisation techniques in volume selected nuclear magnetic resonance spectroscopy. *Phys. Med. Biol* 1990; 35(7):821 – 834
12. Traber F, Block W, Lamerichs R, Gieseke J, Schild HH. ^{1}H Metabolite relaxation times at 3.0 Tesla: Measurements of T_1 and T_2 values in normal brain and determination of regional differences in transverse relaxation. *Journal of Magnetic Resonance Imaging* 2004; 19:537 – 545
13. Ernst T, Kreiss R, Ross BD. Absolute Quantitation of water and metabolites in the human brain. I. Compartments and water. *Journal of Magnetic Resonance* 1993; Series B 102:1 – 8
14. Keevil SF, Newbold MC. The performance of volume selection sequences for *in vivo* NMR spectroscopy: implications for quantitative MRS. *Magnetic Resonance Imaging* 2001; 19:1217 – 1226
15. May, P.A., Brooke, L., Gossage, J.P., Croxford, J., Adnams, C., Jones, K.L., et al. Epidemiology of fetal alcohol syndrome in a South African community in the Western Cape Province. *American Journal of Public Health* 2000; 90:1905 - 1912
16. Croxford, J., & Viljoen, D. Alcohol consumption by pregnant women in the Western Cape. *South African Medical Journal* 1999; 89:962 – 965
17. Jacobson, J.L., Jacobson, S.W, Molteno, C.D., & Odendaal, H. A prospective examination of the incidence of heavy drinking during pregnancy among Cape Coloured South African women. *Alcoholism: Clinical and Experimental Research* 2006b; 30:233A
18. Jacobson SW, Stanton ME, Molteno CD, Burden MJ, Fuller DS, Hoyme HE, et al. Impaired eyeblink conditioning in children with fetal alcohol syndrome. *Alcoholism: Clinical and Experimental Research* 2008; 32:365 – 372
19. Calhoun F, Warren K. Fetal alcohol syndrome: Historical perspectives. *Neuroscience and Biobehavioral Reviews* 2007; 31:168 – 171
20. Jones KL, Smith DW. Recognition of the fetal alcohol syndrome in early infancy. *Lancet* 1973; 2:999 - 1001
21. Hoyme HE, May PA, Kalberg WO, Kodituwakku P, Gossage JP, Trujillo PM, Buckley DG, Miller JH, Aragon AS, Khaole N, Viljoen DL, Jones KL, Robinson

LK. A practical clinical approach to diagnosis of fetal alcohol spectrum disorders: Clarification of the 1996 Institute of Medicine criteria. *Pediatrics* 2005; 115:39 - 47

22. Streissguth AP, O'Malley K. Neuropsyciatric implications and long-term consequences of fetal alcohol spectrum disorders. *Semin. Clin. Neuropsychiatry* 2000; 5:177 - 190
23. Guerri C. Neuroanatomical and neurophysiological mechanisms involved in central nervous system dysfunctions induced by prenatal alcohol exposure. *Alcoholism: Clinical and Experimental Reasearch* 1998; 22(2):304 – 312
24. Spadoni AD, McGee CL, Fryer SL, Riley EP. Neuroimaging and fetal alcohol spectrum disorders. *Neuroscience and Biobehavioral Reviews* 2006; 31:239 - 245
25. Guerri C, Pascual, Renau-Piqueras J. Glia and fetal alcohol syndrome. *NeuroToxicology* 2001; 22:593 – 599
26. Sowell ER, Mattson SN, Thompson PM, Jernigan TL, Riley EP, Toga AW. Mapping callosal morphology and cognitive correlates: Effects of heavy prenatal alcohol exposure. *Neurology* 2001b; 57:235 – 244
27. O'Hare ED, Kan E, Yoshii J, Mattson SN, Riley RP, Thompson PM, et al. Mapping cerebellar vermal morphology and cognitive correlates in prenatal alcohol exposure. *Neuroreport* 2005; 16:1285 - 1290
28. Archibald SL, Fennema-Notestine C, Gamst A, Riley EP, Mattson SN, Jernigan TJ. Brain dysmorphology in individuals with severe prenatal alcohol exposure. *Dev Med Child Neurol* 2001; 43:148 – 154
29. Sowell ER, Thompson PM, Mattson SN, Tessner KD, Jernigan TL, Riley EP, et al. Regional brain shape abnormalities persist into adolescence after heavy prenatal alcohol exposure. *Cereb Cortex* 2002a; 12:856 – 865
30. Sowell ER, Mattson SN, Kan E, Thompson PM, Riley ER, Toga AW. Abnormal cortical thickness and brain-behavior correlation patterns in individuals with heavy prenatal alcohol exposure. *Cereb Cortex* 2008a; 18:126 – 144
31. Bookstein, F.L., Sampson, P.D., Streissguth, A.P., & Connor, P.D. Geometric morphometrics of corpus callosum and subcortical structures in the fetal-alcohol-affected brain. *Teratology* 2001; 64: 4 - 32

32. Ma, X., Coles, C.D., Lynch, M.E., LaConte, S.M., Zurkiya, O., Wang, D., Hu, X. Evaluation of corpus callosum anisotropy in young adults with fetal alcohol syndrome according to diffusion tensor imaging. *Alcoholism: Clinical and Experimental Research* 2005; 29:1214-1222
33. Wozniak, J.R., Mueller, B.A., Chang, P., Muetzel, R.L., Caros, L., & Lim, K.O. Diffusion tensor imaging in children with fetal alcohol spectrum disorders. *Alcoholism: Clinical and Experimental Research* 2006; 30:1799-1806
34. Sowell E, Johnson A, Kan E, et al. Mapping white matter integrity and neurobehavioral correlates in children with fetal alcoholspectrum disorders. *Journal of Neuroscience* 2008; 28(6):1313 - 1319
35. Fryer SL, Tapert SF, Mattson SN, Paulus MP, Spadoni AD, Riley EP. Prenatal alcohol exposure affects frontal-striatal BOLD response during inhibitory control. *Alcoholism: Clinical and Experimental Reasearch.* 2007; 31(8):1415 - 1424.
36. Miller MW, Al-Rabiai S. Effects of prenatal exposure to ethanol on the number of axons in the pyramidal tract of the rat. *Alcoholism: Clinical and Experimental Reasearch* 1994; 18:346 – 354.
37. Astley SJ, Richards T, Aylward EH, Olson HC, Kerns K, Brooks K, Coggins TE, Davies J, Dorn S, Gendler B, Jirikovic T, Kreagel P, Maravilla K. Magnetic resonance spectroscopy outcomes from a comprehensive magnetic resonance study of children with fetal alcohol syndrome. *Magnetic Resonance Imaging* 2009a; 27:760 – 778
38. Astley SJ, Aylward EH, Olson HC, Kerns K, Brooks A, Coggins TE, Davies J, Dorn S, Gendler B, Jirikowic T, Kraegel P, Maravilla K, Richards T. Magnetic resonance imaging outcomes from a comprehensive magnetic resonance study of children with fetal alcohol spectrum disorders. *Alcoholism: Clinical and Experimental Reasearch* 2009b; 33(10):1 – 19
39. Astley SJ, Weinberger E, Shaw DWW, Richards TL, Clarren SK. Magnetic resonance imaging in ethanol exposed Macaca nemestrina. *Neurotoxicology and Teratology* 1995; 17(5):523 – 530
40. Cortese BM, Moore GJ, Bailey BA, Jacobson SW, Delaney-Black V, Hannigan JH. Magnetic Resonance and spectroscopic imaging in prenatal alcohol-exposed

children: preliminary findings in the caudate nucleus. *Neurotoxicology and Teratology* 2006; 28:597 – 606

41. Fagerlund A, Heikkinen S, Autti-Ramo I, Korkman M, Timonen M, Kuusi T, Riley EP, Lundbom N. Brain metabolic alterations in adolescents and your adults with fetal alcohol spectrum disorders. *Alcoholism: Clinical and Experimental Research* 2006; 30:2097 – 2104
42. Herbert, J.S., Eckerman, C.O., & Stanton, M.E. The ontogeny of human learning in delay, longdelay, and trace eyeblink conditioning. *Behavioral Neuroscience* 2003; 117:1196 – 1210
43. Christian, K.M., & Thompson, R.F. Neural substrates of eyeblink conditioning: acquisition and retention. *Learning & Memory* 2003; 10(6):427 – 455
44. Lavond, D.G., & Steinmetz, J.E. Acquisition of classical conditioning without cerebellar cortex. *Behavioural Brain Research* 1989; 33:113 – 164
45. Green, J.T., Tran, T., Steinmetz, J.E., & Goodlett, C.R. Neonatal ethanol produces cerebellar deep nuclear cell loss and correlated disruption of eyeblink conditioning in adult rats. *Brain Research* 2002a; 956:302 – 311
46. Green, J.T., Johnson, T.B., Goodlett, C.R., & Steinmetz, J.E. Eyeblink classical conditioning and interpositus nucleus activity are disrupted in adults rats exposed to ethanol as neonates. *Learning & Memory* 2002b; 9:304 – 320
47. Dunty, W.C., Chen, S., Zucker, R. M., Dehart, D. B., & Sulik, K.K. Selective vulnerability of embryonic cell populations to ethanol-induced apoptosis: Implications for alcohol-related birth defects and neurodevelopmental disorder. *Alcoholism: Clinical and Experimental Research* 2001; 26:1523 – 1535
48. Hamre, K.M., & West, J.R. The effects of timing of ethanol exposure during the brain growth spurt on the number of cerebellar Purkinje cells and granule cell nuclear profiles. *Alcoholism: Clinical and Experimental Research* 1993; 17:610 – 622
49. Dikranian K, Qin YQ, Labruyere J, Nemmers B, Olney JW. Ethanol-induced neuroapoptosis in the developing rodent cerebellum and related brain stem structures. *Developmental Brain Research* 2005; 155(1):1-13

50. Goodlett CR, Horn KH. Mechanisms of alcohol induced damage to the developing nervous system. *Alcohol Reasearch and Health* 2001; 25:175 – 184
51. Valles S, Sancho-Tello M, Minana R, Climent E, Renau-Piqueras J, Guerri C. Glial fibrillary acidic protein expression in rat brain and in radial glia culture is delayed by prenatal ethanol exposure. *J Neurochem* 1996; 67:2425 – 2433
52. Dodge NC, Jacobson JL, Molteno CD, Meintjes EM, Bangalore S, Diwadkar V, Hoyme EH, Robinson LK, Khaole N, Avison MJ, Jacobson SW. Prenatal alcohol exposure and interhemispheric transfer of tactile information: Detroit and Cape Town findings. *Alcoholism: Clinical and Experimental Research* 2009; 33(9):1628 - 1637
53. Astley SJ, Clarren SK. Measuring the facial phenotype of individuals with prenatal alcohol exposure: Correlations with brain dysfunction. *Alcohol & Alcoholism* 2001; 36(2):147 - 159
54. Rooney WD, Johnson G, Li X, Cohen ER, Kim SG, Ugurbil K, Springer CS. Magnetic field and tissue dependencies of human brain longitudinal $^{1}H_20$ relaxation *in vivo*. *Magnetic Resonance in Medicine* 2007; 57:308 – 318
55. Gasparovic C, Yeo R, Mannell M, Ling J, Elgie R, Phillips J, Doezema D, Mayer AR. Neurometabolite concentrations in gray and white matter in mild traumatic brain injury: A 1H–magnetic resonance spectroscopy study. *Journal of Neurotrauma* 2009; 26(10):1635 - 1643
56. SigmaPlot ® 11.0, Systat Software, Inc. San Jose, CA.
57. Harvey BH, Brink CB, Seedat S, Stein DJ. Defining the neuromolecular action of myo-inositol. Application to obsessive-compulsive disorder. *Progress in Neuro-Psychopharmacology & Biological Psychiatry* 2002; 26:21 – 32
58. Elberling TV, Danielsen ER, Rasmussen AK, Feldt-Rasmussen U, Waldemar G, Thomsen C. Reduced myo-inositol and total choline measured with cerebral MRS in acute thyrotoxic Graves' disease. *Neurology* 2003; 60:142 – 145
59. Brand A, Richter-Landsberg C, Leibfritz D. Multinuclear studies on the energy metabolism of glial and neuronal cells. *Developmental Neuroscience* 1993; 15:289 – 298

60. Shimon H, Sobolev Y, Davidson M, Haroutunian V, Belmaker RH, Agam G. Inositol Levels Are Decreased in Postmortem Brain of Schizophrenic Patients. *Society of Biological Psychiatry* 1998; 44:428 – 432
61. Jolles J, Bothmer J, Markerink M, Ravid R. Phosphatidylinositol kinase is reduced in Alzheimer's disease. *J Neurochem* 1992; 58:2326 – 2329
62. Fuchs E, Czéh B, Kole MHP, Michaelis T, Lucassen PJ. Alterations of neuroplasticity in depression: the hippocampus and beyond. *European Neuropsychopharmacology* 2004; 14: S481–S490